3 Electron Cryomicroscopy and Image Reconstruction of Viral Nanoparticles

Bettina Böttcher

CONTENTS

3.1   HISTORICAL BACKGROUND

Historically, the developments in electron microscopy and sample preparation have been closely linked to the structure determination of viral nanoparticles. This is partly due to the high availability of some of these viral nanoparticles and to their high symmetry. Tobacco mosaic virus (TMV) was one of the earliest objects that have been imaged with the electron microscope (Kausche et al. 1939). However, sample preparation methods were still crude and relied on drying of the virus from a low-salt buffer. The drying conditions led to bending and distortions of the virus. Furthermore, the lack of contrast made it difficult to recognize features.

Nevertheless, these very early electron micrographs were already sufficient to measure the length and the width of a typical TMV particle. Later, more sophisticated techniques used coating of the surface of TMV with a thin layer of carbon under a shadowing angle (Matthews et al. 1956). This gave much better contrast and also showed some details on the surface of the virus particle. However, the level of detail was still insufficient to measure the correct distance between repeating units or to identify the general building principles of TMV from its subunits.

At the same time, TMV was also popular in x-ray crystallography for advancing x-ray fiber diffraction (Franklin and Holmes 1958), which resulted in the first density functions of TMV. From these density functions, a model of the organization of the subunit arrangement could be derived (Klug and Caspar 1960). Electron microscopy still lacked behind in suitable preparation methods and thus could not resolve these fine details.

Then, in the late 1950s, Brenner and Horne showed the potential of negative staining for the visualization of viruses (Brenner and Horne 1959). Negative staining was a fast and easy preparation method, which preserved the virus structures relatively well and gave a good contrast with lots of image detail. Micrographs of negatively stained TMV showed a high level of detail (Nixon and Woods 1960) that agreed well with the models derived from x-ray diffraction, which gave confidence in the preparation method.

Although a lot could be learned by just looking at these images, much more could be gained from averaging the information and identifying the characteristic, reoccurring structural features. Since computing was still in its infancy, optical methods had been devised, for optimally superposing different images and averaging them photographically (Markham et al. 1963, 1964). While the methods were quite powerful, finding the optimal superposition was still somewhat subjective and relied on recognizing the optimal fit.

To overcome this limitation, Klug et al. decided to make use of the repeating pattern of helical objects such as TMV, which gives rise to regular lines in a diffraction pattern. To observe this diffraction pattern from electron micrographs, they designed an optical device, which allowed generating a diffraction pattern from an electron micrograph in the back focal plane of an optical lens (Klug and Berger 1964). The diffraction pattern of the image could be reconstructed into an image by adding a second imaging lens (Klug and DeRosier 1966). The device did allow not only observing the diffraction pattern but also manipulating it in the back focal plane, for example, by masking, before reconstructing the image with the second lens. Masking was a very powerful tool for reducing the image information to the components, which were regularly packed in a helix and excluding other contributions, which were mainly added by the noise in the background. Thus, the filtered images were much clearer and could be interpreted with much greater confidence than the unfiltered noisy micrographs. Furthermore, differential masking of the diffraction pattern allowed separating the contributions from the front side of a helical arrangement from the information from the backside. Although this was not yet a 3D image reconstruction, it gave much clearer insights into the 3D building pattern of a helical arrangement. The power of the method was initially demonstrated on TMV and the tail of the bacteriophage T4 (Klug and DeRosier 1966) and then used to elucidate how the structure of bacteriophage T4 changes upon contraction (Krimm and Anderson 1967).

Shortly afterward, DeRosier and Klug (1968) formulated the general principles of image reconstruction in Fourier space and demonstrated its effectiveness on the tail of the bacteriophage T4, for which the helical symmetry of the tail enabled the calculation of a 3D map from a single image. The principle of image reconstruction in Fourier space was later worked out for single particles in general (Crowther et al. 1970b) and developed for the special case of icosahedral symmetry (Crowther 1971). The reconstruction method was applied to various virus structures such as tomato bushy stunt virus, human wart virus (Crowther et al. 1970a), and turnip yellow mosaic virus (Mellema and Amos 1972). The image reconstruction required that the orientation and the origin of a particle relative to the symmetry axes were known. For icosahedral particles, Crowther (1971) came up with a very elegant solution. He showed that in the Fourier transform of a projection, every symmetry axis in the 3D object gives rise to pairs of common lines in the Fourier transform along which the information is the same. The position of the lines changes with the orientation of the object relative to the symmetry axes. Searching for the 37 common lines within a transform of an icosahedral particle was a very elegant and reference-free method for determining the orientation of the particle.

Helical and icosahedral reconstruction methods relied on the fact that the symmetry of the assemblies was well preserved and not distorted by the preparation methods. It soon became apparent that the distortions from perfect symmetry, which were introduced by the staining procedures, severely limited the resolution. This was mainly due to the flattening of the sample during drying and to the uneven staining. So, approaches were devised with which the assemblies could be maintained in an aqueous environment and could be imaged free of stain. First attempts in the early 1970s aimed at lowering the vacuum close to the object and saturating it with water vapor. This allowed imaging wet objects at room temperature. Electron diffraction studies on thin catalase crystals showed that this approach conserved structural details up to 2 Å resolution (Matricardi et al. 1972), which surpassed what could be achieved with stained and dried catalase crystals by almost one order of magnitude. Obviously, retaining the water was essential for obtaining high-resolution structural information.

At about the same time, an alternative route for retaining the water inside the microscope was tested. This approach relied on freezing the sample and imaging it at liquid nitrogen temperature inside the electron microscope (Taylor and Glaeser 1973). At the low temperatures, the vapor pressure of the water dropped below the pressure of the vacuum and thus, evaporation of the sample was efficiently prevented. Freezing proved similarly effective to retain high-resolution

features in catalase crystals (Taylor and Glaeser 1974) as using a differential vacuum system in the column to stabilize a wet sample at room temperature. However, from an instrumentational point of view, cold samples were much easier to handle than a differential vacuum system.

The initial preparation method for unstained cold samples simply relied on freezing the sample in liquid nitrogen. Yet, the cooling rates in liquid nitrogen are relatively low and thus, water crystallizes as hexagonal ice. Soon, it became apparent that the growing ice crystals also had a damaging effect onto the biological specimens. So, it was important to keep the frozen water in a state, which was more like a liquid. In the 1980s, it was demonstrated that a vitrified state of water could be created by rapidly cooling water to low temperatures (Bruggeller and Mayer 1980; Dubochet and McDowall 1981). Electron and x-ray diffraction patterns both showed diffuse diffraction rings of this form of water, similarly as expected for a liquid. Dubochet and coworkers were convinced that this amorphous form of water was the best way to preserve the structures of biological specimens for electron microscopy. They developed efficient ways for the preparation (Lepault and Dubochet 1986) of particles in vitrified suspension (Lepault et al. 1983) and for sections of vitrified, thicker objects (McDowall et al. 1983) such as bacteria (Dubochet et al. 1983). Key to the method development was understanding which phase of water forms under which condition and how the different modifications of water change in the electron microscope (Dubochet and McDowall 1981; Dubochet et al. 1988). Many of the investigated specimens were viruses (Adrian et al. 1984; Vogel et al. 1986; Baschong et al. 1988; Dubochet et al. 1994). The level of detail and the structural preservation, which were achieved by vitrification, were stunning and unprecedented.

In the following years, many low-resolution virus structures were determined using the new preparation technique and the image reconstruction methods based on common lines and Fourier reconstruction developed earlier by Crowther. Initially, most of the structures were determined from very few particles (20–100). Nonetheless, making use of the high symmetry of the icosahedral particles gave structures in the range of 20–40 Å resolution. More importantly, the structures were undisturbed by stain or other preparation artifacts. Gradually, the number of particles in the reconstruction increased and reference-based approaches were incorporated into the determination of particle orientations. Later, methods were developed for correcting for the aberrations introduced by the contrast transfer of the electron microscope. By 1999, some 180 different reconstructions of icosahedrally arranged viral nanoparticles ranging from 25 to 140 nm in size were published (reviewed in Baker et al. 1999).

Many of the reconstructions showed capsids in different states and thus gave valuable structural insights into capsid maturation. In some cases, the resemblance of certain features in the reconstructions to crystal structures of isolated subcomponents was intriguing. So finally the crystal structures of these components were fitted into the respective

entities in the EM maps, giving the first pseudoatomic models (Wang et al. 1992; Olson et al. 1993; Stewart et al. 1993). Although it was not entirely clear at that time, whether this was scientifically justified, it is now a well-accepted and well-advanced technique to combine EM data with high-resolution structural models to build pseudoatomic models of larger complexes.

Virus particles also proved excellent objects for advancing the methods to obtain higher and higher resolution. The first obstacle was to overcome the limitations which were introduced by the contrast transfer function (CTF) of the electron microscope (Figure 3.1, black). Without correcting for it, the position of the first zero in the CTF, which depends on the defocus, also sets the ultimate limit of the obtainable resolution. Since an underfocus of several micrometers was needed to introduce sufficient phase contrast for determining the orientation of the virus particles, finding a solution to the contrast transfer problem was essential for pushing the resolution limit. A correction algorithm was developed with turnip yellow mosaic virus as a test object (Böttcher and Crowther 1996). Together with a slight increase in the number of particles (180), this already increased the resolution to 15 Å, which was a clear leap compared to what was achieved without correction for the CTF.

Another important technological advance for increasing the resolution was the availability of electron microscopes with a field emission gun. These electron sources were much brighter and had superior spatial and chromatic coherence. As a consequence, high-resolution information was transferred much stronger than in electron microscopes with a conventional thermionic source (Figure 3.1, red and blue).

In addition, faster computers and cheap, large computer storage made it possible to process thousands of particles instead of just a few hundred. So, toward the end of the twentieth century, reconstructions of icosahedral capsids with resolutions below 1 nm were determined. These reconstructions resolved α-helices as rod-shaped features (Böttcher et al. 1997; Conway et al. 1997) and for the first time demonstrated that secondary structural elements could be resolved from the reconstructions of single particles. At that point, the image-processing strategies, which led to the high-resolution structures, were specific to icosahedral symmetry. However, in principle an icosahedral particle is nothing else than a special case of a multicopy object (single particle). So, single-particle image-processing packages were further developed and now include all the necessary symmetry operations to obtain high-resolution structural information from multicopy objects of any symmetry.

In 2008, the 4 Å resolution barrier was surpassed on a rotavirus double-layer particle (Zhang et al. 2008). The 3.8 Å resolution map showed a similar level of detail as the crystal structure, which was published later (McClain et al. 2010). By now, single-particle image-processing methods (Grigorieff 2007) were seriously competing with x-ray crystallography in structure determination. At the end of 2013, 16 structures (Yu et al. 2008, 2011, 2013; Zhang et al. 2008, 2010, 2012, 2013a,b; Liu et al. 2010a; McClain et al. 2010; Wolf et al. 2010;
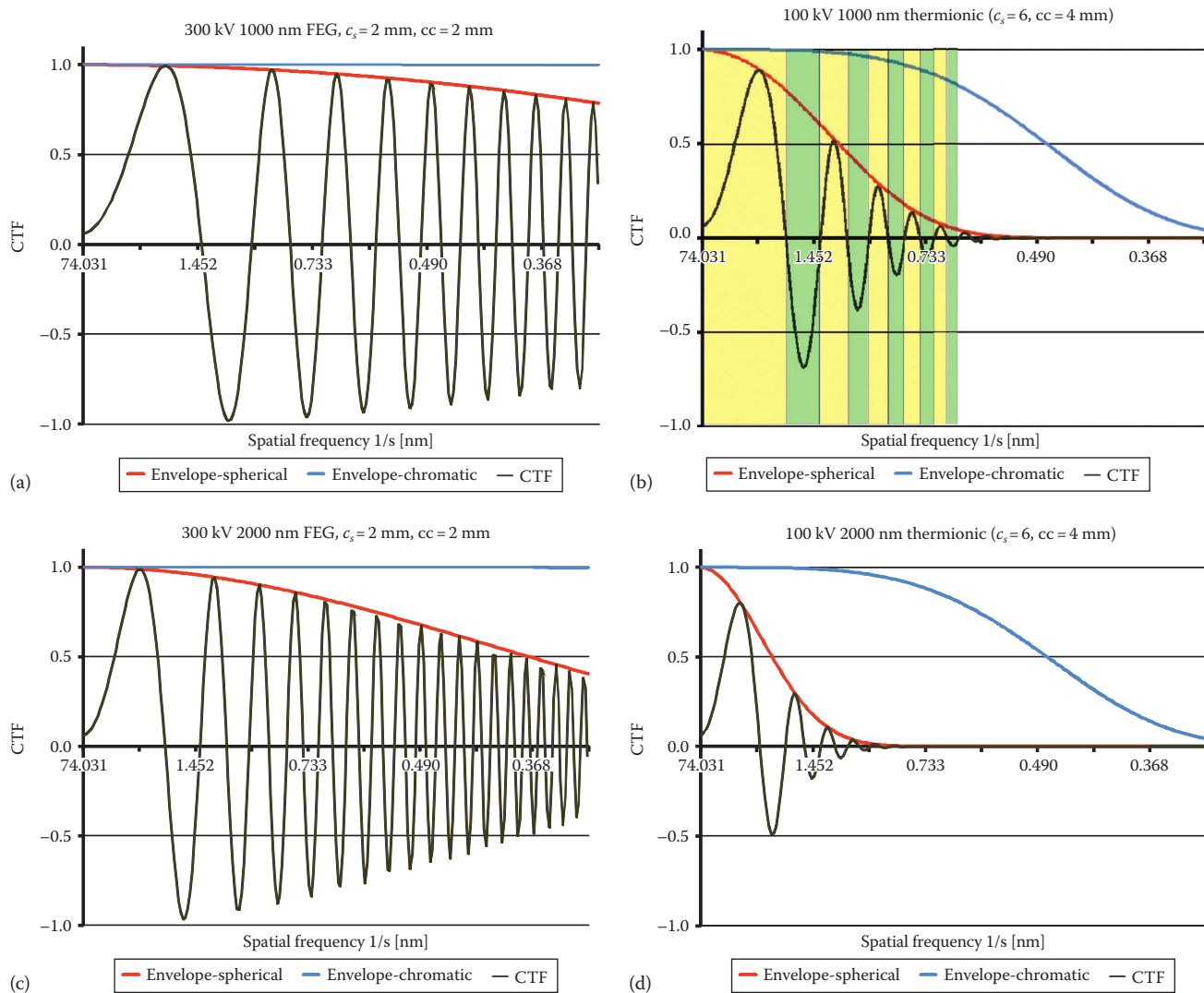
FIGURE 3.1 Contrast transfer function (CTF) for different types of microscopes and for different defocus values. The CTFs (black curves) are modulated by the envelope functions caused by spherical aberration (red curve) and by chromatic aberration (blue curve). (a and c) The CTF for an electron microscope with Schottky field emitter (energy spread 0.7 eV, opening half angle 0.04 mrad) operating at 300 kV and with c_s = 2 mm and cc = 2mm. (b and d) The CTF for a conventional electron microscope with a thermionic electron source (energy spread 1.5 eV, opening half angle 0.25 mrad), and a Biotwin lens (c_s = 6.3 mm and cc = 4 mm) operating at 100 kV. The CTF (black curve) oscillates between +1 and −1 in dependence of the spatial frequency and is dampened by the envelope functions. Different frequency bands are transferred with opposite contrast. In panel (b), the transfer bands with positive contrast transfer are highlighted in yellow and with negative transfer in green. The CTF oscillates faster at larger defocus. The envelope that is imposed by the spherical aberration (red curve) depends on the defocus. In contrast, the envelope that is caused by the chromatic aberration of the electron microscope is independent of the defocus (blue curve). Typically, the main limiting factor is the spherical aberration, while the chromatic aberration is only effective at higher spatial frequencies. Electron microscopes with a thermionic electron source and a large spherical aberration (e.g., Biotwin lens) do not transmit information at 1–2 μm defocus at spatial frequencies >1/7 Å^{-1}, while this range is well transmitted in electron microscopes with a lower spherical aberration (e.g., twin lens or super twin lens) and a Schottky emitter. The diagrams were generated with the Excel sheet created by Stahlberg (2012).

Chen et al. 2011a; Cheng et al. 2011; Settembre et al. 2011) of icosahedral nanoparticles with resolutions better than 4 Å had been deposited in the electron microscopy data bank (EMDB, Henrick et al. 2003; Lawson et al. 2011).

Although computing power was greatly improved and more coherent electron sources were available, high-resolution work still used photographic film as primary detector. Out of the 16 maps of icosahedral nanoparticles that were reconstructed to resolutions better than 4 Å, 15 relied on data from

film as primary detector. Film has a much better transfer of fine details as the conventional CCD cameras (Figure 3.2) that require conversion of the incident electrons into a detectable light signal. In 2009, the first direct detectors for electron microscopy became available (McMullan et al. 2009a,b). It became quickly apparent that they had the potential to outperform film for electrons at 300 kV accelerating voltage. Furthermore, the fast read-out rates of direct detectors allowed recording movies rather than single, high-dose images.
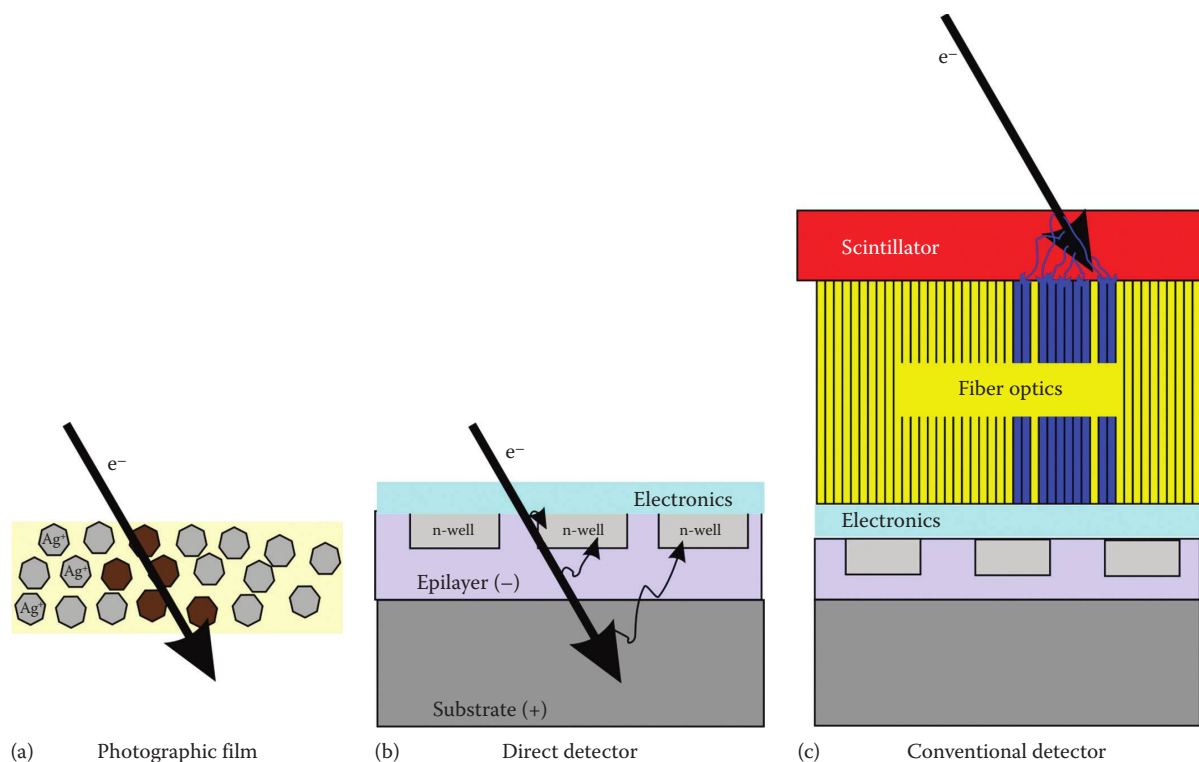
FIGURE 3.2 Detectors in electron microscopes: (a) photographic film contains silver halide grains in a gelatin layer. The size of the grains (gray) is <1 µm and the thickness of the gelatin layer (yellow) is in the order of 25 µm. The incident electrons enter the sensitive layer and change the properties of the grains, which makes them convertible into silver in the subsequent developing process. One electron can change the properties of several grains (amplification of the signal). High-energy electrons are partly back scattered by the film carrier and reenter the sensitive layer at a different position, which leads to an increase in unspecific background. (b) A direct detector consists of several layers. The upper layer contains the electronic read-out circuits and is some 2–4 µm thick. The read-out is located on top of the n-wells in the epilayer (5–25 µm thick). The incident electron generates many hole–electron pairs in the epilayer (signal amplification). The electrons of these electron–hole pairs diffuse toward the n-wells where they change the read-out signal. The substrate layer (up to 500 µm thick) underneath the epilayer acts as a potential barrier, which cannot be entered by the electron–hole pairs. Nevertheless, the substrate layer can be entered by the incident electrons, which have a much higher energy. In the substrate layer, these electrons are partly back scattered and reenter the epilayer at a different position, producing more electron–hole pairs and adding to the background noise. The problem is reduced by back-thinning the substrate layer. The incident electron also passes through the read-out electronics, where it causes damage to the electronics. Therefore, direct detectors have the potential problem of a limited lifetime due to radiation damage. (c) In a conventional electronic detector, the incident electrons pass through a scintillator layer, where they excite emission of many photons across a relatively large area (amplification of the signal). The light signal is passed through fiber optics to the electronic detector, which can be either a CMOS or a CCD detector. Similar as in direct detectors, the photons generate electron–hole pairs that change the read-out signal of the pixels. The photons have much lower energy than the incident electrons in a direct detector. Therefore, a photon typically generates only one single electron–hole pair. Since the electronics of the direct detector is not directly exposed to the high-energy incident electrons, damage to the read-out electronics is not a problem in conventional detectors.

These movies showed beam-induced movement of the particles in the vitrified water (Brilot et al. 2012). The movement degraded the high-resolution image information in a conventional high-dose image. However, in a movie, the independent movement of the particles could be corrected in the individual frames, and thus, the image quality could be greatly improved (Li et al. 2013). Now, it has been demonstrated that with the advent of the new detectors and electron microscopes with automated loading systems for the sample and fully or semi-automated data collection, structures with resolutions better than 4 Å can be acquired within days. This provides a bright future for structure determination of icosahedral nanoparticles and suggests that for these types of assemblies, x-ray crystallography will become largely obsolete.

The analysis of helical particles made a similar rapid progress over the past years. At the beginning of the twenty-first century, researchers made use of iterative helical real-space refinement (Egelman 2000; Sachse et al. 2007). This enabled much more accurate determination of the orientation of small helical patches and thus correcting for small deviations from perfect helical symmetry in the whole helical assembly (e.g., bending of the helical tube). As a result, resolution in helical reconstructions improved fast either by using real-space refinement methods or alternatively by using standard crystallographic procedures. At the end of 2013, there were five helical structures deposited in the electron microscopy database (acetylcholine receptor; Unwin 2005, bacterial L-type flagella;

Maki-Yonekura et al. 2010, and three of TMV; Sachse et al. 2007; Clare and Orlova 2010; Ge and Zhou 2011) with resolutions better than 5 Å.

3.2 SAMPLE PREPARATION

High-resolution structure determination of viral nanoparticles by electron microscopy requires a preparation method, which preserves the whole structure of the nanoparticle in an aqueous surrounding without any staining. The method of choice is vitrification of a particle suspension and has been introduced by Dubochet and coworkers in the 1980s (for review see Dubochet et al. 1988; Dubochet 2012).

Vitrified samples are typically prepared by applying a suspension of nanoparticles onto a sample carrier either directly as small droplets (spraying) or by forming a thin film by removal of most of the sample (e.g., by blotting with filter paper). Afterward, the sample together with its carrier is plunged into a cryogen, which rapidly cools the sample below the vitrification temperature of approximately −137°C. High cooling rates (10^{-4} K/s) support the vitrification of the water, whereas slower cooling rates lead to the formation of hexagonal, crystalline ice. The vitrified state is unstable above temperatures of approximately −120°C (Mayer and Bruggeller 1983) but stable for at least 5 min at temperatures below −137°C (Dubochet et al. 1988). Irradiation with electrons in the electron microscope can also induce devitrification at lower temperatures above −150°C (Heide 1984). To preserve the vitrified state, samples are stored in liquid nitrogen and require permanent cooling during sample handling, sample transfer, and sample imaging.

The success of sample preparation depends on several factors, which include the sample carrier, the method of film formation (spraying vs. blotting), and the choice of cryogen. These factors will be discussed in the following.

3.2.1 Sample Carriers

Standard electron microscopy holders accept round grids with a diameter of 3.05 mm, which are available in different materials (e.g., Cu, Cu/Rh, Al, Ti, Au, Mo, Ni, Be). For biological applications, copper or copper/rhodium grids are most commonly used. The grids have a metal surface with either square, round, or hexagonal openings in defined distances. The pitch between openings is given by the mesh size, which is the number of openings per inch. A typical mesh size for the preparation of vitrified samples is 400 mesh, which corresponds to a pitch of 63.5 μm with a typical side length of the opening of 35–40 μm.

Normally, grids are coated with carbon support film (1–40 nm thick), which consists of amorphous carbon that has a high mechanical strength, is inert to most solvents used in biology, and is largely translucent for electrons. These properties make amorphous carbon film an ideal support for electron microscopy. In addition, amorphous carbon has some electrical conductance at liquid nitrogen temperature, which helps to dissipate charges that build up during imaging. Thick carbon

support films (10–40 nm) also have good mechanical stability, which decreases beam-induced movement. However, thick carbon films also scatter electrons much more strongly than thin carbon films and give rise to a grainy background that superimposes with the image of the nanoparticle. The problem is reduced by decreasing the thickness of the carbon support film to 1–2 nm. However, these very thin carbon films are no longer stable on their own over large areas and easily rupture when the sample is applied or when the film is irradiated with electrons. To overcome this problem, a thick carbon support film with holes (typical diameter of the holes 1–5 μm) is used as a carrier, which is coated with an additional, thinner, continuous carbon layer. Now, the thin, continuous carbon film only needs to be self-supporting over the small areas of the holes, where the nanoparticles are imaged.

An alternative to thin carbon film is graphene, which is a different modification of carbon, and has been discovered only a decade ago (Novoselov et al. 2004; Meyer et al. 2007). Graphene is one layer of carbon-atoms thick and forms extended 2D crystals, which are extremely sturdy in respect to their thickness. In addition, the conductivity of graphene per mass is significantly higher than that of amorphous carbon. First experiments have shown that the background added by a graphene support film is indeed minimal and allows the identification of unstained DNA, which is impossible with other support films (Pantelic et al. 2011). Graphene is also sturdy enough to support larger biological complexes (Pantelic et al. 2012). However, the preparation of large self-supporting graphene films is still difficult and thus, it is not yet routinely available as a support film for electron cryomicroscopy. An alternative to grapheme is graphene oxide (Wilson et al. 2009). The additional oxygens at the surface provide a hydrophilic surface that interacts well with the particle suspension. Graphene oxide is easier to produce than graphene and is now commercially available as additional support film on holey carbon-coated grids.

Holey carbon support films are also used without additional continuous carbon support films. In this case, a self-supporting particle suspension with a thickness of approximately 20–100 nm is formed across the holes, where the unsupported nanoparticles can be imaged. This has the advantage that the viral nanoparticles are not deformed by absorption to a support film and that no additional background is added by the support film to the image of the nanoparticles. The drawback is that unsupported holey films are somewhat more labile and give rise to more beam-induced movement during imaging. Despite the increased beam-induced movement, high-resolution (<4 Å) structures have been determined from unsupported viral nanoparticles (e.g., rotavirus [Zhang et al. 2008], cytoplasmic polyhedrosis virus [Yu et al. 2011], or TMV [Ge and Zhou 2011]).

Most applications use holey carbon films either with or without an additional support layer. There are various lab protocols for generating the required holey carbon films, which rely on generating a plastic film with holes as a template. The holes are either generated by condensation of little water droplets on a surface, which exclude the plastic film from these areas (Murray and Ward 1987) or by including bubbles of an immiscible liquid

into a solution of plastic, which then give rise to holes in the plastic film after etching (Harris 1962; Bayer and Anderson 1963; Moharir and Prakash 1975; Baumeister and Seredynski 1976). The holey plastic film serves as a template onto which the thick carbon layer is evaporated. Finally, the plastic film is dissolved in organic solvent and a holey carbon film remains. The resulting pattern of holes and the size distributions of holes are irregular. These irregularities are a major obstacle for automated data acquisition schemes, which are more efficient with regular hole patterns and with diameters of the holes that are adapted to the illuminated area or the size of the detector. Regular hole patterns require a controlled pattering algorithm, which is achieved by photolithography either with a consumable soft template that is dissolved (Ermantraut et al. 1998; Chester et al. 2007) or with a hard template and a water-soluble release layer to replicate the pattern onto the carbon film (Quispe et al. 2007). Grids with such patterned holey support films are commercially available from different suppliers with different hole sizes, hole shapes, and hole patterns.

Shortly after evaporation, carbon films are hydrophilic but become more and more hydrophobic and thus water repellent over time. If an aqueous particle suspension is applied onto such hydrophobic carbon film, the suspension interacts very little with the support film and does not wet it properly. Therefore, vitrified samples prepared with hydrophobic grids are often either too dry or the particle suspension is too thick. The hydrophobicity and thus the wettability of the carbon support film can be increased by exposing it to a plasma immediately before use. The plasma is formed by passing an electrical current through a low pressure gas, which leads to a glow discharge. This generates radicals of the gas, which change the surface properties of the exposed surfaces, in this case the properties of the support film. While glow discharge with *air* as gas deposits negative charges onto the amorphous carbon film, an atmosphere of amylamine adds positive charges to the surface (Dubochet et al. 1971). Glow discharge increases the wettability of amorphous carbon and lowers the contact angle between the carbon surface and water droplets (Kutsay et al. 2008). This facilitates easy spreading of a particle suspension and is essential for the formation of a thin, homogeneous particle film. The increase in wettability by glow discharge is reversible and is completely reverted after some 2 h (Kutsay et al. 2008). The choice of positive or negative charges or the use of freshly floated carbon gives a wide range of different surface properties, which have subtle influence on the distribution of the nanoparticles and to some extent, also, on the orientation of the particles on the support film.

Amorphous carbon has a different thermal expansion coefficient to the supporting copper grids. As a consequence, the copper grids shrink much more upon cooling than the carbon support film does, which leads to severe folds in the carbon support film and tensions in the vitrified sample. This phenomenon was described by Booy and coworkers as cryocrinkling of the carbon film (Booy and Pawley 1993). Cryocrinkling is reduced by using a grid material with a lower expansion coefficient such as molybdenum or titanium (Booy and Pawley 1993; Vonck 2000).

3.2.2 Formation of Thin Particle Suspensions

High-resolution imaging of vitrified viral nanoparticles requires that they are contained in a very thin film of their vitrified buffer on the sample carrier. Ideally, the thickness of the film is approximately the same thickness as the diameter of the particles. Thicker films give reduced contrast and increase the percentage of electrons, which are scattered inelastically or multiple times. Depending on the size of the particle, a useful thickness of a vitrified suspension is approximately 20–200 nm.

3.2.3 Blotting and Evaporation

Typically, thin films are formed by applying the sample to a grid with or without support film and then removing excess liquid. The process of film formation is quenched by plunging the grid with the particle suspension into a cryogen (Figure 3.3). In this method, two processes contribute to the removal of the liquid: one is the absorption of the liquid to the filter paper and the other is the evaporation of the water from the sample. The latter gives rise to a decrease in the temperature of the sample and an increase in the concentration of the particles and solutes. Depending on the environment, evaporation is rapid and can be the major driving force of the film formation (Trinick and Cooper 1990). While the increase in the number of particles during evaporation is often advantageous (e.g., for dilute particle suspensions), the increase in the concentration of solutes and especially of salts is unwanted and can interfere with the integrity and/or conformation of the nanoparticles.

The speed of evaporation is influenced by the ambient temperature and the relative humidity in the surroundings (Frederik and Hubert 2005) as well as the concentration of the solutes and the surface area, which is accessible to evaporation during film formation. An experimental setup without control of these parameters in the microenvironment of the sample requires some experience to identify the right moment, when the film has the optimal thickness before quenching the film formation by plunging the grid into the cryogen. To reduce this random factor, many devices control humidity as well as the temperature in the local environment of the sample. By increasing the humidity to almost 100%, evaporation can be virtually stopped. The simplest way to generate an environment with 100% humidity is to bubble air through water before blowing it onto the grid (Dubochet et al. 1988; Cyrklaff et al. 1990). A more sophisticated approach is to surround the sample with a chamber with a fully controlled environment inside (Bellare et al. 1988) (Figure 3.3). The chamber can be humidified with water-soaked sponges, which have a large surface area for exchange of water vapor with the surrounding or by using an ultrasonic nebulizer (Frederik and Hubert 2005). Inside the chamber, it is also possible to control the temperature either by heating or by cooling with a Peltier element. This gives full control of the major environmental parameters that influence the evaporation rate and enables reproducible sample preparation with very little optimization of other factors.
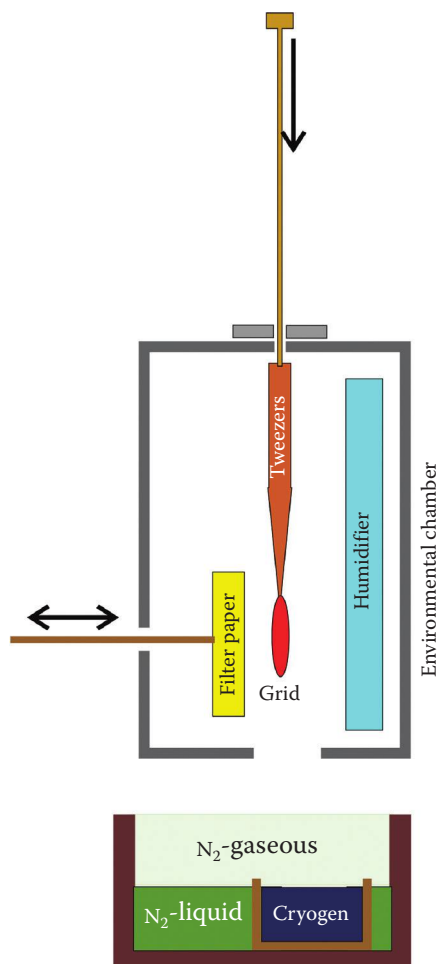
FIGURE 3.3 Schematic drawing of a manual freezing apparatus similar to the Bellare design (Bellare et al. 1988). The grid (red) is held by a pair of tweezers (brown) that is connected to a movable rod. The rod together with the grid and the tweezers can be propelled (gravity, spring, and motor) toward the cryogen. During blotting, the grid is surrounded by an environmental chamber (gray), which is humidified by a humidifier (e.g., wet sponge or ultrasonic nebulizer). The thin film of the sample is formed by coplanar blotting with filter paper (yellow). For blotting, the filter paper can be moved with a rod that is accessible from the outside of the chamber. After film formation, the grid is plunged into the cryogen. The cryogen (ethane, propane, or a mixture of both) is placed in a small vessel that is surrounded by a larger vessel, which contains liquid nitrogen and an atmosphere of cold, dry nitrogen gas.

The other process, which contributes to the formation of the thin film, is the active removal of excess liquid by blotting with filter paper. Again, there are many factors that influence the outcome of the blotting process. They include the type of filter paper, the force with which the filter paper is applied, the blotting time, the contact area and the contact angle between the filter paper and the sample, and the direction of blotting. Blotting can be done either from the same side as the sample was applied to or from the opposite side (Toyoshima 1989) or simultaneously from both sides. Blotting from both sides has the advantage that there is no exposed surface area of the grid,

from which the solvent can evaporate. This makes it unnecessary to control the humidity in the microenvironment of the grid, because the sample is humidified from both sides by the wet filter paper (Cyrklaff et al. 1990; Trinick and Cooper 1990). Devices with double-sided blotting are realized either in self-built plunging devices or in computer-controlled devices such as the FEI-Vitrobot, the Gatan Cryo plunge, or the time-resolved freezing apparatus from White and coworkers (Walker et al. 1995; White et al. 1998). Blotting single sided from the front or back gives similarly good results. Single-sided blotting from the back (opposite to where the sample was applied) minimizes the contact area between nanoparticles and the filter paper. In some cases, this helps to increase the number of particles in the field of view (Toyoshima 1989). Most manual devices use single-sided blotting, but there are also fully computer-controlled, commercial cryoplungers such as the Leica EM GP that support single-sided blotting. In single-sided blotting, the surface-accessible area of the grid is much larger than in double-sided blotting and thus, evaporation is a major factor, which requires a controlled microenvironment for reproducible results as described earlier.

Another important aspect is the contact angle between the sample and the filter paper. In most blotting devices, grid and filter paper are oriented coplanar, which gives the maximal contact across the whole area of the grid. This leads to an even film thickness across the grid. Therefore, coplanar blotting results in the largest possible area with optimal sample thickness, if optimal blotting conditions are found. The disadvantage is that if the blotting conditions are not optimal, the whole grid is likely to be suboptimal. For that reason, a few devices such as the FEI-Vitrobot use a design where the filter paper touches the grid under an angle. This generates a gradient in the strength of the contact between the filter paper and the sample across the whole grid. As a consequence, the thickness of the film is also variable across the grid, leaving some areas with an optimal thickness of the film even if the blotting conditions are not optimized yet. However, after optimization of the conditions, a typical film has still extended areas that are either too thin or too thick for imaging. Furthermore, since mounting of the grid in the device can vary by some ±0.5 mm, the area with the optimal thickness is not always centered, which is problematic for applications such as tomography that requires optimal sample thickness in the center of the grid for recording images at large tilt angles.

In addition to the contact angle between filter paper and grid, blot time and blot force are also important. Blotting too strongly often leads to a completely dry grid. Here, the sample appears to be mechanically ripped off the grid rather than being slowly absorbed into the filter paper. With more moderate blot forces, where blotting is controlled by the absorption of the solution into the filter paper rather than by a mechanical manipulation of the film, useful blotting times are less critical in a controlled microenvironment. Successful blotting times between 1 and 20 s have been reported.

The filter paper itself also influences the result of the blotting process. Filter papers come with different flow

rates, which are related to how fast they can blot off the sample from the grid. For forming thin films, filter papers with medium to medium–fast flow rates like Whatman No. 1 (medium flow rate, 11 μm particle retention) or Whatman No. 595 (medium fast, 4–7 μm particle retention) are most commonly used, while filter papers with slow flow rates are uncommon for the formation of thin films in vitrification experiments.

Filter papers also vary in their composition. Standard filter papers have significant amounts of trace elements that can dissolve and enter the sample. In particular, the most commonly used Whatman No. 1 contains 0.13 mg calcium/g filter paper. This calcium is enough to change the conformation of calcium-sensitive assemblies. If sensitivity to trace elements is an issue, ashless filter papers with similar flow rates are a better alternative (e.g., Whatman No. 40, 42, or 43).

A variant of the preparation of thin films by blotting is the bare-grid method. Here, grids are used without further support film (Adrian et al. 1984; Dubochet et al. 1988; Jager 1990). In this method, the excess liquid is blotted off the grids and film formation is followed through binoculars and terminated by plunging the grid into a suitable cryogen (ethane or propane) when the film starts to rupture. Thus, the method uses a mixture of sample removal by blotting and evaporation. The preparation method requires some experience for recognizing the right moment for terminating the process of the film formation. In the bare-grid method, the film thickness varies across the grid, because the thickness partly depends on the gravity-driven flow of the water and thus increases toward the bottom of the grid.

In the bare-grid method, the size of a mesh that is spanned without further support is some 30–50 μm for a 400 mesh grid, which requires a relatively thick film to form a stable, self-supporting particle suspension. The suspension is typically thicker toward the grid bars and thinner in the center of a mesh. A problem of samples prepared by the bare-grid method is that the unsupported suspensions are nonconducting; therefore, they rapidly charge up during irradiation with electrons, which leads to image blurring. Although the bare grid method has been used for structure determination in the past (Adrian et al. 1984; Schatz et al. 1995), it is now no longer considered as suitable for high-resolution studies. Nonetheless, the method might have its merits for very large nanoparticles that get easily distorted by interactions with support films or by the pressure in very thin suspensions.

3.2.4 Spraying

An alternative for removing excess sample by blotting and evaporation is depositing a film of suitable thickness in the form of tiny droplets directly onto the grid. This is achieved by spraying microdroplets onto the support film of a grid while it is plunged into the cryogen (Dubochet et al. 1982). For the formation of a thin film, very small droplets are required, which still cover areas of 1–2 μm^2. Such droplets are generated by sprayers or *atomizers*. However, on a hydrophobic surface (such as an untreated carbon support film), droplets of this size do not spread and thus, they produce a film, which is far too thick for imaging. To facilitate rapid spreading of the drops after impact, the surface of the grid has to be extremely hydrophilic (glow discharge). But even with all the parameters carefully adjusted, the thickness of the droplets is still variable across each droplet, with a thick center and a thinner outer rim. Furthermore, with the impacting drops spaced some micrometers apart, a significant part of the surface of the grid remains dry, which further reduces the useful area. Therefore, spraying has lost its importance as a standard procedure for preparing thin films for vitrification.

On the other hand, spraying has the potential of starting a reaction by spraying an agent onto the sample just before quenching the reaction by vitrification. Thus, it is an ideal approach for time-resolved electron cryomicroscopy. The concept has been further developed by Berriman and Unwin for imaging the acetylcholine receptor in the open state (Berriman and Unwin 1994). In contrast to the spraying method described previously, Berriman and Unwin first formed the thin film of the acetylcholine receptor by conventional blotting (see previous text) and then sprayed the agent (acetylcholine) onto this preformed, thin film during plunging. This method requires a tight coupling of the action of the sprayer with the plunging of the grid via a photoswitch and enables reactions times of 1–100 ms.

The spreading of droplets on a preformed, thin film is far more efficient than spraying the droplets onto a dry grid. This is likely due to the fact that the already formed film and the impacting droplets have similar surface properties and therefore mix easily. While large particles such as viruses or ferritin remain within the boundaries of the impacting droplet, small solutes, such as ions, diffuse much faster and can be traced outside the impact zone of the drop. Depending on the delay between spraying and freezing, ions can travel several micrometers beyond the boundaries of the drop before the sample is vitrified.

A device that sprays an agent onto the grid allows only the addition of one component and has a very short time interval between the start of a reaction and its quenching, which is determined by the time it takes for the grid after blotting to reach the cryogen. For a more sophisticated control over the time course of a reaction, two mixing chambers are added in front of the spraying device, which allow mixing of different reagents and a free choice of delay times (Walker et al. 1995; White et al. 1998; Lu et al. 2009). Such devices implement a classical quench flow experiment into sample preparation by quenching the reaction by vitrification.

3.2.5 Vitrification

Immediately after forming the thin film by blotting or spraying, the film is stabilized against evaporation by rapid *freezing*. For vitrification, the sample is plunged into a cryogen with a guillotine-like apparatus that is either driven by

gravity, accelerated by a spring, moved by pneumatics, or propelled with a motor. The choice of the cryogen is far more critical than the plunging mechanism and is decisive whether hexagonal ice is obtained or a vitrified sample. Vitrification is only achieved when the cooling rates are high and the sample is rapidly (10^4 K/s) cooled below the vitrification temperature. Although liquid nitrogen is suitable for cooling the sample below this temperature, its cooling rate is far too slow. The reason is the Leidenfrost phenomenon, which was discovered in the eighteenth century. It occurs when a *hot* object is emerged into a liquid, which has a boiling point of a least 100 K below the temperature of the hot object. The large difference in temperature causes film boiling at the surface of the hot object and the formation of an insulating gas layer. The heat transfer across this gas layer is slow, and thus, the *hot* object cools down relatively slowly. The boiling temperature of liquid nitrogen is −196°C and that of the *hot* sample is between 0°C and 40°C. This leads to film boiling and thus to a slow heat transfer, which gives the water time to rearrange and to form crystalline ice rather than vitrified water.

To achieve faster cooling rates, it is essential to use a cryogen, which has a higher boiling point but is still liquid below the vitrification temperature. Such cryogens are ethane, propane, or a 60:40 mixture of both (Tivol et al. 2008) (Table 3.1). The cryogen of choice is condensed into a small reservoir that is cooled with a surrounding bath of liquid nitrogen (Figure 3.3). Unfortunately, the melting points of ethane and propane are above the temperature of liquid nitrogen. Therefore, after a while, these cryogens freeze, and have to be melted again to make them ready for a new round of plunge-freezing grids without mechanical damage of the grids by impacting onto the frozen cryogen. To keep propane or ethane stably in the liquid phase, they have to be periodically warmed by condensing more gaseous cryogen into the reservoir, or by thermally insulating the reservoir from the surrounding liquid nitrogen bath or by heating the reservoir with a heater. Alternatively to ethane or propane, a mixture of both can be used, which forms a eutectic system that freezes at around −196°C and hence stays liquid even when it is cooled with liquid nitrogen (Tivol et al. 2008).

After plunging the sample into the cryogen, the sample is immediately vitrified and can be removed from the cryogen for storage or for transfer to the electron microscope. To keep the grids below the devitrification temperature, they are stored in liquid nitrogen and handled either in liquid nitrogen or in an atmosphere of cold, dry nitrogen gas.

TABLE 3.1
Boiling and Melting Points of Some Cryogens

Cryogen	Boiling Point (K)	Melting Point (K)
Nitrogen	77	66
Ethane	185	90
Propane	231	86
60:40 mixture of ethane/propane	185–231	77

3.2.6 STRATEGIES FOR ON-GRID CONCENTRATION OF VIRAL NANOPARTICLES

Often viral nanoparticles cannot be produced with concentrations that give sufficient particles in the field of view for efficient imaging. To obtain 100 particles in a field of view of 1 μm² in a film with a thickness of 50 nm, a concentration of approximately 3 μM or 2×10^{15} particles/mL is needed. For many viral nanoparticles, these concentrations are out of reach and require concentrating the nanoparticles in situ on the grid.

Occasionally, more particles than expected from the particle concentration are observed in the field of view. Sometimes, the enrichment can be explained by partial evaporation of the solution in an uncontrolled freezing device. In other cases, this seems to be unlikely, because a humidified environmental chamber has reduced evaporation during sample preparation, suggesting that other processes are involved in concentrating the sample on the grid. One of the likely mechanisms is that the nanoparticles move much slower and therefore enter the filter paper far slower than the buffer (water, salts, and other small molecules). Another effect is that nanoparticles enrich at the air–water interface of drops (Johnson and Gregory 1993). The enrichment is slow (minutes to hours) and depends on the size of the particles and the diameter of the drop. Surface enrichment can be utilized to trap virus particles at the air–water interface and to generate a high local concentration of the nanoparticles, which is transferred by touching the surface of the drop with the grid.

Another process that is utilized for enriching viral nanoparticles is to adsorb them onto a thin support film. For example, adeno-associated virus can is enriched by almost a magnitude, when absorbed onto a carbon film (Kronenberg et al. 2001). Other nanoparticles might be trapped on the grid by using functionalized support films such as *the affinity grid* (Ni-NTA-lipids absorbed to a carbon-coated grid; Kelly et al. 2008, 2010) or streptavidin-functionalized graphene oxide support films (Liu et al. 2010c).

3.3 DATA ACQUISITION

There are two fundamentally different types of objects: one type of object exists in multiple, identical copies, and the other is an object with a unique structure. While for multicopy objects, image information from different particles can be merged into a single representative 3D structure, for unique objects, all structural information has to be obtained from one object. This requires different data acquisition schemes for multicopy objects and for unique objects.

3.3.1 DATA ACQUISITION FOR VIRAL NANOPARTICLES IN MULTIPLE, IDENTICAL COPIES

For multicopy objects, micrographs of many different copies of the object from different areas of the sample are acquired. Each micrograph is taken with the maximal, permissible dose

that does not destroy the features at the desired resolution but gives the best possible signal-to-noise ratio. Typically, doses between 5 and 25 electrons/$Å^2$ are used for vitrified samples. These doses are a compromise between optimal contrast at low spatial frequencies (high dose), which is required for determining the accurate orientations of the particles, and the preservation of high-resolution features (low dose). Systematic dose studies of diffraction patterns of 2D bacteriorhodopsin crystals suggest that the maximal permissible dose that preserves high-resolution features at 3 Å at temperatures of about −175°C is approximately 3 e/$Å^2$ (Stark et al. 1996) and that low-resolution image information around 40 Å is already significantly reduced at a dose of 30 e/$Å^2$ (Toyoshima and Unwin 1988; Conway et al. 1993). The optimal signal-to-noise ratio up to 3 Å resolution at an accelerating voltage of 200 kV is obtained at a dose of 10 e/$Å^2$ (Baker et al. 2010).

3.3.2 Low-Dose Imaging

Low-dose imaging techniques minimize the dose on the object and thus reduce beam damage (Unwin and Henderson 1975). All low-dose acquisition schemes include several steps, which consist of searching, positioning, focusing, and acquisition (Figure 3.4): The first step is to search the area of interest at a low magnification and with a low dose ($\ll$0.5 e/$Å^2$). The search step can include information at different magnifications. For example at low magnification (100–400), the whole grid is inspected to identify regions with the most suitable ice thickness and the least surface contamination. Then, at a somewhat higher magnification (1000–5000), meshes are identified with holes that are covered with a homogeneous, thin film of vitrified sample. At this magnification, smaller nanoparticles ($\ll$50 nm) cannot be recognized as individual particles and the choice of the area is purely based on the properties of the vitrified film.

In the next step, the area of interest is centered as precisely as possible for the later image acquisition. This also happens at low magnification but sometimes at a somewhat higher magnification than the actual search process to allow for more accurate positioning. The third step is focusing and waiting for the drift to settle. This requires a higher dose and a higher magnification than the searching and positioning. Therefore, the image shift capabilities of the microscope are used to deflect the beam away (1–5 µm) from the area of interest. There, the beam is focused to illuminate only a small area, avoiding preexposure of the area of interest. For determining and adjusting the defocus and for measuring the specimen drift, the magnification is also increased to recognize finer details such as the graininess of the supporting carbon film. Typically, a defocus of 1–5 µm underfocus is chosen for unstained vitrified multicopy objects. Drift rates are also measured and should be lower than around 1–2 Å/s depending on the targeted resolution and the exposure time. The final step is recording a micrograph of the area of interest: This requires resetting the image shift to the center of the area of interest and

adjusting the beam diameter and the magnification to the desired values. Finally, the beam is centered on the area of interest that is tightly coordinated with the shutter of the detector in order to irradiate the sample only during image acquisition.

3.3.3 Automated Image Acquisition

Most electron microscopes have assisted low-dose acquisition schemes that control image shifts, beam shifts, changes in magnification, changes in illumination, and the operation of the beam shutter coupled with the detector. Despite these sophisticated schemes, low-dose data acquisition is tiring for the operator and thus limits manual acquisition times to a couple of hours. Fortunately, the different steps of low-dose data acquisition are highly repetitive and structured, and thus are an ideal task for computer-assisted automation. Nowadays, there are several acquisition packages that acquire images of the desired areas without any further user intervention (e.g., leginon, autoem, em-Tools, tom2, SAM, EPU; Zhang et al. 2003; Lei and Frank 2005; Suloway et al. 2005; Shi et al. 2008; Korinek et al. 2011). These acquisition schemes run stably and can acquire thousands of micrographs from a single grid over a couple of days. Furthermore, with electronic detectors, the micrographs are already in an electronic format and thus are immediately ready for further image processing. This allows feeding image information directly into the acquisition process and using it for automatic, accurate alignment and positioning.

3.3.4 Considerations for Acquiring High-Resolution Micrographs

The automated data acquisition on electronic detectors has generated a quantum leap in the availability of image data. The increase in high-quality image data allows researchers to address more demanding projects, which require more images to achieve higher resolution, to identify different conformational states in a population of particles, or to work with less abundant particles.

Many images of a large number of different copies of nanoparticles are a prerequisite for addressing problems that are related to the statistics of the particle population. For example, subpopulations in a noisy dataset can be more reliably identified, in a large dataset ($\gg$10,000 per subpopulation) than in a small dataset ($\ll$5000). However, an increase in the amount of data is not necessarily sufficient for obtaining high-resolution (<4 Å) reconstructions. These reconstructions are only obtained if the high-resolution information is present in the micrographs. Various factors reduce the transfer of the high-resolution image information. These factors can be separated into factors that are related to the hardware of the electron microscope (e.g., coherence of the electron source, correction of lens aberrations), the detector (e.g., sensitivity and modulation transfer function of the detector), the stability of the cryoholder, the stability of the environment (e.g., vibrations,
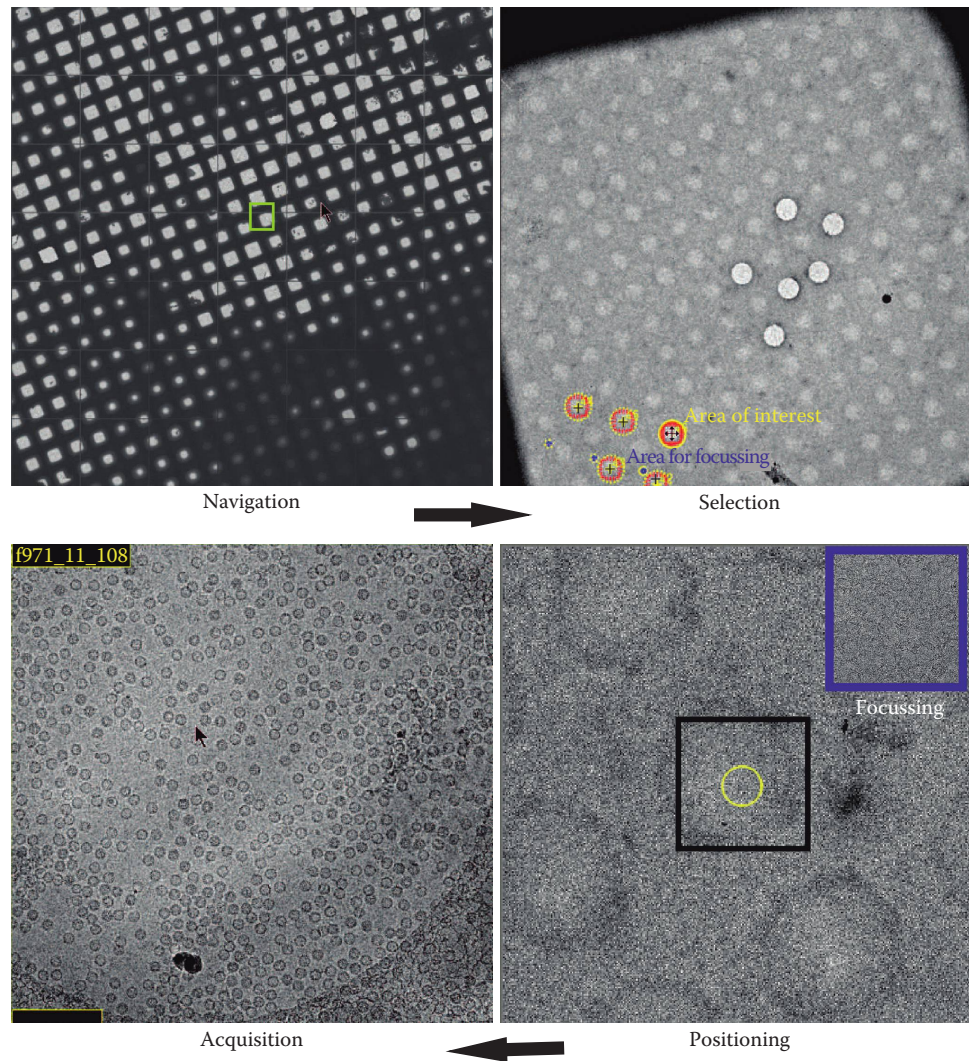
FIGURE 3.4 Semiautomatic low-dose data acquisition. Low-dose data acquisition requires taking images at different magnifications and doses. Upper left panel: A low magnification map of the whole grid allows easy navigation. The grid map also reveals areas with a suitable thickness of the ice. In this example, the ice is too thick for high-resolution data acquisition in the lower right corner of the grid. The grid map is used to identify meshes, which are suitable for further image acquisition. At a magnification of 1000–2000, images of appropriate meshes are acquired (upper right panel), which are used for selecting the areas of interest. The areas of interest are manually selected, avoiding contaminated holes or holes that are not covered with ice. In the upper right panel, some selected areas are outlined with a yellow square and a red circle. The corresponding areas for focusing are highlighted by blue circle. Focusing areas are positioned away from the area of interest. For exact positioning of the area of interest, images at somewhat higher magnification are taken (red outline, lower right panel). These images are cross-correlated with the selected area in the selection image and inform on stage shift and image shift for optimal positioning of the area of interest. This is followed by focusing in the focus area (blue inset, at somewhat higher magnification, typically the same magnification as for the image acquisition). Finally, the image of the area of interest is taken at the desired magnification and the desired dose (lower left panel, black outline). All images were acquired with TVIPS EM-Tools as part of semiautomatic data acquisition.

temperature stability, and absence of electromagnetic fields in the room), the alignment of the electron microscope, and the movement of the particles during image acquisition. While most of these factors cannot be influenced during image acquisition, alignment of the microscope and to some extent detecting the movement of the particles can be addressed during image processing.

It is generally important that the electron microscope is well aligned to recover high-resolution information. Images should be acquired with the sample at the eucentric height where the object is in focus at the optimal lens current of the objective lens. Deviations from the eucentric height lead to changes in the absolute magnification and in image rotation. It is necessary to check and readjust the eucentric height

during image acquisition whenever the position has changed by several tens of micrometers (e.g., when moving from one mesh to the next) to keep the eucentric height accurate within 1–2 μm.

Another limiting factor is the electron-beam tilt (Glaeser et al. 2011; Zhang and Hong Zhou 2011), which arises from deviations of the direction of the beam from the optical axis. Electron-beam tilt can be corrected by coma-free alignment (Zemlin et al. 1978) and is minimized by using parallel illumination (Glaeser et al. 2011; Zhang and Hong Zhou 2011). The electron-beam tilt induces a resolution-dependent phase shift that is larger at lower accelerating voltages. The dependence of the phase shift from the spatial frequency is cubic, and thus, it is the main limiting factor of the phase information at large spatial frequencies (high resolution).

Even if the microscope is perfectly aligned and has the appropriate specifications to record high-resolution image information, it is impossible to record high-resolution image information when the object moves during the image acquisition. This movement can either be a directional movement, which is caused by specimen drift, or it is a random movement that is induced by the irradiation with electrons and subsequent charging, beam damage, and heating of the sample. While the directional movement typically ceases after a while, the beam-induced movement occurs during low-dose imaging and is proportional to the applied dose (Chen et al. 2008; Brilot et al. 2012). Its occurrence cannot be avoided by any known imaging or sample preparation technique although it might be somewhat lower at a low-dose rate (1.5 e/$Å^2$ s) (Chen et al. 2008) or on a thicker carbon support film. A way forward for correcting for the beam-induced movement is to record movies rather than single high-dose micrographs. Movies allow correcting for the beam-induced movement of each individual particle in every movie frame (Brilot et al. 2012). The correction requires that frames are recorded fast and that the total imaging time remains short (1–2 s) so that particle movement is predominantly due to beam-induced, random movement rather than to drift-induced directional displacement. With short total recording times, the average over all frames is comparable to a conventional high-dose image that contains the high-contrast information for the accurate determination of the orientation and position of the particles. The dose of the individual frames is typically low and is in the order of 1 e/$Å^2$ or less. Therefore, the signal-to-noise ratio of the individual frames is not sufficient to determine the relative position and orientation of the particles with the accuracy that is required to compensate for the beam-induced movement (Bai et al. 2013). However, the relative alignment of the frames can be improved by computing sliding averages of several frames rather than using individual frames (Brilot et al. 2012) or by using priors about the likely changes in position and orientation in the alignment process (Bai et al. 2013). With the same data, processing of movies gives significantly better resolution than processing the high-dose averages (Bai et al. 2013).

3.3.5 Data Acquisition of Unique Viral Nanoparticles (Tomography)

For a unique object, all the image information for reconstructing the 3D map has to be taken from the same object by recording a tilt series. A tilt range of 180° is required for recovering the complete 3D information. However, it is practically impossible to observe image information over this whole tilt range, because at higher tilt angles, the area of interest becomes occluded by protruding parts of the specimen holder and the thickness of the irradiated sample increases with increasing tilt angle (factor two at 63°). Both factors limit the practical tilt range to approximately 140° (±70°), but often, the tilt range is even lower. This limitation in angular coverage leads to missing information in the z-direction (parallel to the electron beam) of the reconstruction, which is reduced by a double tilt experiment, in which two complete tilt series are acquired with the tilt axes being oriented approximately perpendicular to each other. This requires rotating the specimen in plane by 90° before recording the second tilt series. The in-plane rotation is supported by a special tilt holder and thus can be done inside the electron microscope without remounting the grid.

Similar as for multicopy objects, the total dose with which the object is imaged is closely related to the achievable resolution. Since all the information comes from a single object, the total dose needs to be sufficient to detect features above the noise level at a certain resolution but at the same time needs to be low enough not to destroy these features by beam damage. In the best case, the achievable resolution in a tomogram is around 20 Å (Henderson 2004) but is often considerably worse. This means that in a tomogram, it is not necessary to preserve structural details at spatial frequencies beyond 1/20 $Å^{-1}$ and total doses of 40–100 e/$Å^2$ are typically used for recording the whole tilt series. Therefore, for recording a tilt series in a tilt range of +70° to −70° in 1° steps with a total dose of 100 e/$Å^2$, a dose of only 0.7 e/$Å^2$ is permitted for each tilt image.

Another consideration is that the individual micrographs of a tilt series have to be aligned to a common origin and the orientation of the tilt axis as well as of the actual tilt angle has to be determined for reconstructing the 3D map. Due to the low signal-to-noise ratio in the individual micrographs of the series, the determination of these parameters is often inaccurate when it is solely based on cross-correlation. For improving alignment, electron-dense colloidal gold particles of 5–20 nm diameter are added to the sample as fiducial markers. But even with fiducial markers, accurate alignment of the tilt images still requires 1–2 e/Å per micrograph (Kourkoutis et al. 2012). To further increase the transfer of image information at low spatial frequencies, micrographs are taken with an underfocus of several micrometers (typical values −5 to −10 μm), which is much higher than for high-resolution studies of multicopy objects.

A different aspect of recording the tilt series is how many equally spaced projections n across the whole tilt range of

180° are required to record the complete information for a certain resolution *d*. The number of tilt images depends on the size of the object *D* and is given by the Crowther criterion (Crowther et al. 1970b):

$$n = \frac{\pi D}{d}.$$

From this equation, the tilt increment α in degree is derived as

$$\alpha = \frac{180 \cdot d}{\pi D}.$$

Thus, for acquiring the complete information of an object of 100 nm diameter at 20 Å resolution, the required tilt increment is approximately 1°.

To minimize the electron dose on the object, a similar low-dose acquisition scheme is used as for multicopy objects. The area of interest is identified and centered at low magnification. The sample is focused at higher magnification away from the area of interest. For tilted objects, the focus area and the area of interest have to be placed precisely on the tilt axis, because otherwise, the focus in the focus area and in the area of interest would differ. After the micrograph is recorded for a certain tilt angle, the object is tilted to the next tilt position. Often the change in tilt leads to some displacement of the area of interest and therefore, focusing and positioning is repeated. The displacement is minimized, when the sample is exactly at the eucentric height. However, imperfections in the goniometer as well as specimen drift often leave residual displacements. To correct for these displacements, the stage and/or the image is shifted to keep the same focus area centered during the whole tilt series. The procedure of compensating for displacement after tilting is referred to as tracking and is an essential step of tomographic data acquisition.

Nowadays, tomographic image acquisition is fully automated and the procedures take care of tracking, focusing and drift checks as well as of low-dose data acquisition. There are several tomographic acquisition packages, which are either commercially available (e.g., Gatan Tomography package, TVIPS EM-Tools, Xplore 3D of FEI) or have been developed by academics (e.g., TOM, Serial EM, Leginon, UCSF tomo) (Fung et al. 1996; Mastronarde 2005; Suloway et al. 2005; Korinek et al. 2011). The automatic acquisition of a tilt series in small angular intervals, over a large tilt range, can take several hours, especially when low drift rates and accurate tracking and focusing are required.

For recording a high-resolution tilt series of a unique object, there are also stringent requirements for the alignment of the microscope. The most important requirement is that the object is exactly at the eucentric height and that the focus area and the area of interest are exactly on the tilt axis. This is important to minimize displacements and changes in focus during image acquisition. Another important factor is a parallel illumination to minimize changes in magnification with changes in defocus, which can amount to inaccuracies of several angstroms across the micrograph (Fan et al. 1995).

3.4 INSTRUMENTATION

A critical issue for imaging viral nanoparticles at highest possible resolution is the adequate instrumentation, which enables recovering high-resolution image information with a good signal-to-noise ratio. There are several elements in an electron microscope that increase the information transfer at certain spatial frequencies. These elements include emitters, sample holders, energy filters, phase plates, aberration correctors, and detectors. Their importance depends on the targeted resolution and the application and will be discussed in the following.

3.4.1 EMITTERS

The main mechanism of contrast formation in vitrified samples is the phase contrast, which depends on differences in the density in the denser object (typically protein, DNA, RNA) and the surrounding, less dense, vitrified buffer. These differences are small, and thus, the phase contrast is also small. To increase the phase contrast at low spatial frequencies, images are often taken at a considerable defocus (depending on the application between −1 and −10 μm). However, taking highly defocused images also has two major implications: (1) Due to the oscillation of the CTF, certain bands of spatial frequencies are transferred with opposite contrast and others are not transferred at all (Figure 3.1). The frequency-dependent change in contrast leads to a delocalization of the image information and has to be corrected during image processing. (2) The contrast transfer at higher spatial frequencies is dampened by an envelope function (Wade 1992). This envelope function depends on the spatial and chromatic coherence of the electron source, the spherical and chromatic aberration of the electron microscope, the wavelength of the electrons, and the defocus. Conventional thermionic electron sources generate electrons by heating an emitter (e.g., tungsten wire, LaB_6 crystal) to overcome the workfunction. Thus, the emitting surface of the source is relatively large, and therefore, the spatial coherence is low. Also the high temperature that is required to overcome the workfunction leads to a considerable energy spread of the exiting electrons (1.5–4 eV), which contributes to the chromatic aberration. As a consequence of the limited coherence at dose rates of 10–20 e/Å^2 s and a defocus of several micrometers, higher-resolution information (<10 Å) is transferred too weakly to be recovered. Hence, acquisition of data close to atomic resolution requires electron sources with high spatial coherence such as Schottky field emitters or cold field emitters. For both types of emitters, the electron emission is assisted by an external field, which is generated by an additional extraction voltage of a few kilovolts. A field of sufficient strength is only generated at the pointed tip of the electron source, which reduces emission to a very small area of the emitter and thus increases the spatial coherence. For cold field emitters, the emission is achieved by the field alone, which requires an almost atomically sharp tip of the electron source for generating a strong enough field. This is in contrast to Schottky emitters that have a somewhat less pointed tip, and therefore, the extraction voltage on its own is not sufficient to cause emission. In this case, the field only decreases the workfunction of the

emitter and the emission is assisted by additional heating of the emitter. In this respect, a Schottky field emitter is not a true field emitter but a field-assisted, thermionic emitter. Similar to cold field emitters, emission only occurs at the tip of the emitter where the field is strong enough.

Although cold field emitters have the best spatial and chromatic coherence, they have been rarely used in transmission electron microscopy of biological specimens. The main reason is that they require a much higher ambient vacuum and contaminate easily, which leads to large fluctuations in their brightness. Cold field emitters require frequent decontamination that is incompatible with high-throughput data acquisition. While the use of field emitters (Schottky or cold) is essential for electron microscopy of vitrified multicopy objects at subnanometer resolution, it is not required for tomographic applications, for which the resolution in a tomogram does not realistically extend beyond 20 Å.

3.4.2 Energy Filters

Often unique objects are considerably larger than multicopy objects, and therefore, the imaged samples can be several hundreds of nanometers thick. In these thick samples, many electrons have undergone inelastic scattering (mean free path of electrons in vitrified buffer at 120 kV is 203 nm; Grimm et al. 1996) and have deposited some of their energy onto the sample. This leads to an energy loss and electrons are no longer properly focused by the lens system of the electron microscope. Image details are blurred and significantly reduced in contrast. A way forward is to remove electrons, which have lost energy from the optical path by an energy filter. This leaves only unscattered and elastically scattered electron in the optical path (zero-loss imaging).

Energy filters are based on the fact that electrons with different energies are differentially deflected in a magnetic field. By using a magnetic field to disperse the electrons according to their energy and a slit aperture, electrons can be selected based on their energy. Energy filters are placed at different positions in the optical path. Some electron microscope manufacturer such as Zeiss and Jeol have developed layouts with the energy filter in-column, whereas Gatan developed a system that is placed post-column and thus can be retrofitted to almost any electron microscope. Both in-column and post-column filers are useful for zero-loss imaging as required for tomographic applications of thicker specimens. By removing electrons from the optical path, energy filters add an additional amplitude contrast (Angert et al. 2000), which also increases the transfer of low spatial frequencies. Therefore, energy filters give an essential improvement of image contrast in tomography, but they are less commonly used for acquiring high-resolution image information of multicopy objects.

3.4.3 Phase Plates

Electron tomography requires strong contrast transfer at low spatial frequencies. Nevertheless, contrast transfer at low spatial frequencies is relatively weak due to the fact that the predominant phase contrast transfer follows a sine function. To increase the transfer at low spatial frequencies, one option is to increase the defocus, which shifts the first maximum of the CTF toward lower spatial frequencies but also introduces contrast reversals at lower spatial frequencies (Figure 3.1). Alternatively, the proportion of amplitude contrast can be increased by using energy filtering (see Section 3.4.2). However, both measures are unsatisfactory for contrast recovery at very low spatial frequencies. To overcome this limitation, phase plates have been proposed, which are similar to Zernike phase plates in light optical microscopy (Zernike 1942). These phase plates shift the phase of the scattered electrons by 90°, which results in optimal contrast transfer at low spatial frequencies (conversion of a sine dependency of contrast transfer into a cosine dependency). Zernike-type phase plates are located in the back-focal plane and are realized by a thin carbon film with a small hole. The hole is aligned in such a way that the unscattered electron beam passes through it and the scattered electrons pass through the carbon, where their phases are shifted by approximately 90° due to the interaction with the carbon film. The smallest spatial frequency that is affected by the phase shift decreases with the size of the hole, and this is in the order of $1/140$–$1/160$ nm^{-1} for retrofitted phase plates (Marko et al. 2011).

Experiments on T4 phage have demonstrated a huge increase in image contrast close to focus and have proven that the phase plate delivers the expected contrast increase for low spatial frequencies (Danev et al. 2010). For image reconstructions of multicopy objects, a significant increase in contrast is observed, and as a consequence, only 30%–50% of particles are required to achieve a certain resolution (Murata et al. 2010). The benefit of the phase plates is demonstrated up to subnanometer resolution.

3.4.4 Spherical Aberration Corrector

Spherical aberration of the objective lens induces an additional frequency-dependent phase shift. For biological low-resolution applications, this is exploited for obtaining more contrast at low spatial frequencies close to focus, by using objective lenses with a very large spherical aberration (e.g., FEI Biotwin lens with a c_s of 6.3 mm). However, such a large spherical aberration also limits the point-to-point resolution of the electron microscope and causes faster defocus-dependent degradation of the contrast transfer at higher spatial frequencies (Figure 3.1). The spherical aberration can be corrected by a c_s-corrector, which allows adjusting c_s values over a wide range. A c_s-value of zero increases the point resolution of the electron microscope and improves contrast transfer at high spatial frequencies. These improvements are essential for material science applications where subangstrom resolution is required. At first glance, the benefits for biological applications, which target much lower resolution (3–4 Å), are less obvious. Here, a c_s of zero also sets the phase shift, which is introduced by electron-beam tilt (e.g., nonoptimal alignment and/or nonparallel illumination) to zero (Zhang and Hong Zhou 2011). Therefore, it is

likely that c_s-correctors will improve the resolution of biological applications, for which electron-beam tilt is one of the major limiting factors for obtaining high-resolution image reconstructions.

3.4.5 DETECTORS

For many years, photographic film has been the most efficient detector for recording high-resolution electron micrographs. Film provides an excellent spatial resolution, because it has a large field of view and electrons are detected directly by changing the properties of the fine grain of the film emulsion (Figure 3.2a). Indeed, most of the image reconstructions at resolutions better than 4 Å have been recorded on film (Yu et al. 2008; Zhang et al. 2008, 2010, 2012, 2013a,b; Liu et al. 2010a; Wolf et al. 2010; Chen et al. 2011; Settembre et al. 2011; Yu et al. 2011, 2013). However, the sensitivity and linearity of the response to electrons is poor, the handling is inconvenient, and the data can only be used for further image analysis after time-consuming processing (developing, drying, and scanning of film).

For a long time, an alternative to film has been conventional CCD or CMOS detectors (Figure 3.2c). These detectors measure a light signal, which comes from a scintillator that is excited by the incident electrons. The light signal is transmitted to the sensor either by a fiber-optical coupling or by an optical lens. A major limitation is that the area of the scintillator that is excited by one electron is relatively large. This leads to a delocalization of the information and thus to an unfavorable point spread function, which limits the resolution. The typical quantum efficiencies of a conventional CCD or CMOS detector at 0.5 of the Nyquist frequency are 0.1–0.3, depending on the voltage (better for lower accelerating voltage; quantum efficiency at Nyquist frequency are 0.01–0.07) (Ruskin et al. 2013). To compensate for the delocalization of the signal and the weak contrast transfer close to Nyquist frequency, micrographs are recorded at a higher magnification as would be used for data acquisition on film. Unfortunately, this reduces the field of view to a fraction of what can be imaged with a similar spatial resolution on film.

The advantage of conventional CCD or CMOS detectors is the better linearity in dose response over a wider dynamic range with higher sensitivity. Furthermore, electronic detectors deliver micrographs in a digital format almost instantly. This is a prerequisite for automated, computer-controlled data acquisition such as tomography and automated multicopy particle image acquisition, which relies on feeding back image information into the alignment and positioning process.

More recently, direct CMOS detectors were developed. Other than conventional CCD and CMOS detectors, they do not use a scintillator for converting electrons into a detectable light signal, but directly detect the charge separation caused by the incident electrons in the epilayer of the detector (Figure 3.2b). Thus, the blurring of the signal is less extended and at accelerating voltages above 200 kV, direct detectors outperform conventional CCD or CMOS detectors (Ruskin et al. 2013). A further advantage of the new direct detectors is their

rapid read-out. Rather than recording a single micrograph, it is possible to record the image information as a movie with some 20 frames per second. This allows computational correction of beam-induced movement in the subsequent image processing (Campbell et al. 2012; Bai et al. 2013).

Some of the direct detectors have an even faster read-out that enables counting of individual electrons rather than integrating the signal. Counting increases the linearity of the dose response and thus improves the resolution. Furthermore, by detecting single electrons, the position of the incident electrons can be determined with subpixel resolution, which gives superresolution information beyond the Nyquist frequency (Gatan K2 summit).

3.5 IMAGE PROCESSING

As outlined earlier, there are unique objects and multicopy objects, which have different requirements not only for the data acquisition but also for the subsequent image processing and the expected resolutions. For unique objects, the optimal resolution is determined by the beam damage of the sample and the signal-to-noise ratio at a certain spatial frequency. These considerations suggest that the resolution can probably not exceed 20 Å (Henderson 2004). For multicopy objects, there is no theoretical limitation that prevents achieving atomic resolution. In theory, averaging a few thousand particle images should already be sufficient to reconstruct a structure of a multicopy object at a resolution of approximately 3 Å (Henderson 1995) in the absence of any image degradation. In reality, two to three orders of magnitude more asymmetric units need to be processed and averaged to recover structural information beyond 4 Å resolution. This suggests that electron microscopic images are far from perfect.

Image processing aims at combining the different projections of the object that have been generated by the electron microscope in a consistent way into a 3D map and to correct for the image distortions imposed by the electron microscope and the detector.

3.5.1 IMAGE RECONSTRUCTION OF MULTICOPY OBJECTS

Historically, very different approaches have been used for different types of multicopy objects. For particles with icosahedral and helical symmetry, certain symmetry-related properties of the Fourier transforms have been exploited for determining the particle orientations. These specialized approaches cannot be used for asymmetric multicopy objects, which always require the comparison with other images (e.g., reference images of a noise-free reference or other images of a different view of the object) for determining the relative orientations of the particles. Nowadays, the specialized approaches for helical and icosahedral objects are mainly used for the determination of a first model, which is followed by more general image-processing strategies that are independent of the symmetry.

These general strategies have a common workflow, which includes four steps: (1) Preprocessing: The image data are

prepared for further image processing. This includes windowing of the individual particle images from the micrographs and determining the parameters of the CTF of the microscope for every micrograph. (2) Determination of the orientations of the particles: This can be done either ab initio or by comparison of the particle image with a common reference. (3) Image reconstruction: The 3D map of the object is calculated by combining all 2D particle images with the correct orientation into a 3D map. Typically, the determination of the orientations is an iterative process, in which the current best 3D map serves as reference map for the reference-based determination of particle orientations. (4) Postprocessing: The final 3D map is corrected for the attenuation of high spatial frequency information.

3.5.1.1 Preprocessing of the Image Data

Image processing of multicopy objects requires a set of images with equal size, in which each image contains one copy of the multicopy object. To generate this set of particle images, the positions of the particles on the micrographs are determined either by selecting the desired particles manually or automatically, by using certain properties of the local modulation of the gray value distributions or by correlation with reference projections. After identifying the positions of the particles in the micrographs, the particles are extracted into smaller particle images that are somewhat larger than the particle diameter (approximately two times the particle diameter) and contain one particle per image. For further image processing, the particle images are normalized in their gray value distribution.

Automatic approaches to particle selection often incorporate false-positive particle images (e.g., ice contaminations, edge of the illuminated area or edge of the hole), which contain high-contrast features. Therefore, automatically selected datasets require a stringent postsorting process, which uses different parameters for recognizing the particles than the parameters that have been used for the automatic particle selection. One strategy is the reference-free classification in which false-positives typically do not group into well-defined classes and do not align with high accuracy. Particle images from such ill-defined classes are excluded from further processing.

Preprocessing of the particle images often includes further steps such as tight masking of the particles with a smooth mask, band-pass filtration, the inversion of the gray values, and the correction for the CTF. The accurate determination of the CTF (Figure 3.1) and its correction is critical for obtaining high-resolution image reconstructions. Without correction of the CTF, the image information would not average coherently and the gray value distribution of the object would be misrepresented in the final map. A very successful approach to the determination of the CTF is ctffind3 (Mindell and Grigorieff 2003), which divides the whole micrograph into smaller patches, and averages the power spectra of these patches. After a background correction of the averaged power spectra, the cross-correlation to a simulated power spectrum in a given frequency band is maximized. The method works reliably and can determine the parameters of the CTF more accurately than most curve fitting approaches in which the density profile of a background subtracted power spectrum is

fitted with the CTF. The determined parameters are incorporated into other programs for further correction of the contrast transfer of the microscope either during preprocessing or later, during image reconstruction.

3.5.1.2 Determination of the Orientations

The extraction of particle images is followed by the determination of the orientations relative to a 3D reference map. This can be done by cross-correlating the particle image to a set of projections of this 3D reference map. The particle image is assigned with the same orientations as the best correlating reference projection. However, for a fine angular sampling, the comparison requires a huge number of reference projections and thus can be computationally ineffective.

Alternatively, a limited number of equally spaced reference projections are computed. In Fourier space, the Fourier transforms of these reference projections define a fixed network of intersecting planes (Figure 3.5). The Fourier transform of the particle image intersects with this network of intersecting planes along certain lines. Along these intersecting lines, the information in the Fourier transforms of the reference projection and in the transform of the particle projection is the same. The position of the intersecting lines depends only on the orientation of the particle and on the orientation of the reference projections. The particle image is assigned with the orientation for which the predicted intersecting lines in the Fourier transforms of the reference projections and in the particle transform have the highest correlation. This method is referred to as cross common line method (Crowther 1971) and has the advantage that finer angular sampling does not require a larger number of reference projections.

The cross common line approach is particularly powerful for icosahedral particles, for which the symmetry gives rise to 60 cross common lines for each transform of a reference projection (Crowther 1971; Crowther et al. 1994). The incorporation of the symmetry in the search also helps to focus the determination of orientations on the icosahedrally related elements. This is, for example, helpful, when the icosahedral organization of a viral nanoparticle is determined, which contains asymmetric components (e.g., packaged genome, attached packaging proteins).

3.5.1.3 Helical Assemblies

A special case of multicopy objects are helical assemblies, for which the asymmetric unit is related by a radial distance to the helical axis, a rotation angle around the helical axis and by an axial rise. Other than for conventional multicopy objects, the particle images are not the whole helical assembly, but overlapping helical segments. For these segments, in projection, a shift along the helical axis has the same effect as a rotation around the helical axis. Therefore, the shift along the helical axis is restricted in search space, whereas full rotation around the helical axis and a limited tilt ($\pm15°$) of the helical axis out of plane are permitted (Egelman 2000, 2010; Sachse et al. 2007). By identifying the angular orientation and the origin of each helical segment, it is possible to correct for slight deviations from the perfect helical symmetry as would occur
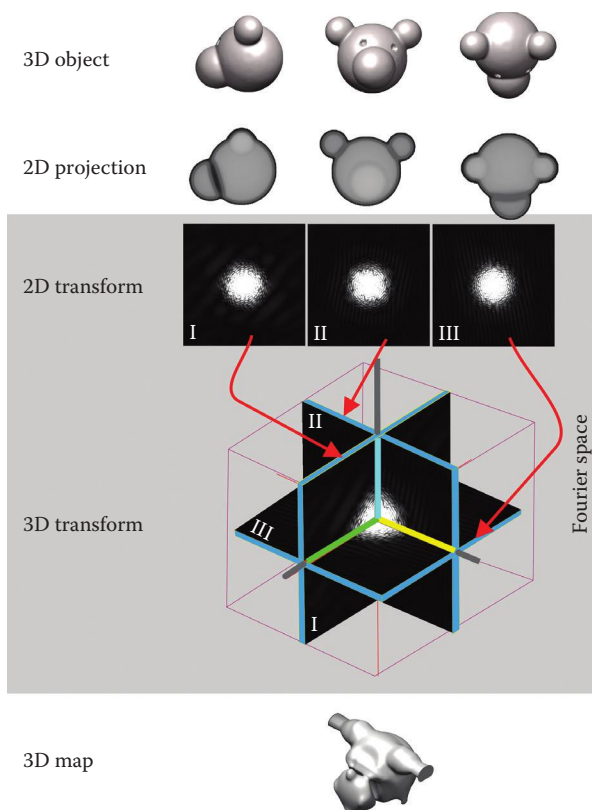
the low-resolution information of the reference map for orientational searches of the full asymmetric unit on a coarse angular grid. After the overall orientation of a particle is established, local searches on a finer angular grid follow, which include the higher spatial frequencies. This strategy helps to find reliable orientations that are not dominated by noise correlation, which often occurs if high-frequency information is included in the iterative refinement.

3.5.1.5 Reconstruction of the 3D Map of the Object

After the orientations of the particle images have been determined, the 3D structure of the particle is reconstructed. Image reconstruction can be done in real space or in Fourier space. Real-space algorithms include weighted back-projection, algebraic reconstruction techniques (ARTs), and statistical image reconstruction techniques (SIRTs).

Alternatively, reconstructions can also be calculated in Fourier space followed by Fourier inversion. Some of the approaches have been specifically adapted for icosahedral nanoparticles or particles with rotational symmetry and use spherical harmonics (Crowther 1971; Navaza 2003; Liu et al. 2008a; Estrozi and Navaza 2010) in Fourier space. In the following, only the two general approaches of Fourier inversion and weighted back-projection will be discussed:

3.5.1.5.1 Fourier Inversion

In electron microscopy, a particle image corresponds to a projection of the 3D particle. The 2D Fourier transform of such a particle projection is a section through the 3D Fourier transform of the particle (Figure 3.5). The orientation of the section in Fourier space depends on the orientation of the particle in real space. All sections go through the origin of the 3D Fourier transform. By adding 2D Fourier transforms of many different views of the particle, the 3D Fourier space is evenly sampled. Since the grid points of the sections and the grid points of the 3D Fourier transform do not necessarily coincide, a proper Fourier interpolation scheme has to be implemented (Grigorieff 2007) to minimize the oversampling of the low spatial frequencies. Finally, the real-space 3D map is calculated by transforming the 3D Fourier transform into real space (Fourier inversion).

The advantage of combining the image data in Fourier space is that image information is represented as a function of spatial frequencies. Therefore, it is simple to manipulate frequency-dependent modulations such as the CTF of the microscope or the frequency-dependent degradation of the image information. In Fourier space, these factors can be conveniently deconvoluted with appropriate frequency-dependent filter functions. Especially the correction of the CTF is effectively done during image reconstruction in Fourier space by multiplying the Fourier transforms of the individual particle images F_i with the respective CTFs c_i and summing the products in the 3D Fourier transform F. The multiplication downweighs weakly transferred data in the averaged transform but misrepresents the amplitudes. In real space, such a map without further correction of the amplitudes would appear somewhat skinny and would overestimate cavities. Therefore, for a quantitative representation of

FIGURE 3.5 Principle of image reconstruction in Fourier space: The object (upper row) has different orientations in respect to the incident beam. In this example, the object is rotated by 90° around its *X*- and *Y*-axes. The microscope generates 2D projections of the object (second row). These 2D projections are transformed into 2D Fourier transforms (third row, labeled I, II, III). The 2D Fourier transforms are section of the 3D transform of the object (fourth row). The sections go through the origin of the transform and have the same relative orientations as the object had relative to the incident beam (in this case perpendicular). The sections intersect along certain lines (blue between I and II, yellow between II and III, and green between I and III). Along these lines, the information of intersecting transforms is the same. These lines are referred to as cross common lines and can be used for determining the orientation of a particle. The image is reconstructed by inverse transforming the 3D Fourier transform that includes all the 2D Fourier transforms into real space (fifth row, surface representation of the reconstruction calculated from the three projections shown in the second row).

by bending of the helical tube. For shorter helical segments, imperfections in the helical symmetry can be more accurately corrected. However, shorter segments also contain less information, and therefore, their orientation is less precisely determined than for longer helical segments. Thus, the resolution of the final reconstruction of a helical assembly depends critically on the chosen length of the helical segments.

3.5.1.4 General Considerations for the Determination of Orientations

The low spatial frequencies ($<1/20$ Å^{-1}) are most important for the determination of the relative orientations of the particle images. Therefore, some search strategies use only

the density of the particle in the 3D map, it is also essential to correct the amplitudes. The amplitudes are restored by dividing the sum of the Fourier components by the summed square of the CTF values. Furthermore, an additional weighting factor w_i can be introduced that weights images based on their properties (e.g., signal-to-noise ratio). Finally, to reduce overrepresentation of globally, weakly transferred data, a Wiener weighting factor f is included (Böttcher and Crowther 1996; Grigorieff 2007):

$$F = \frac{\sum_i c_i w_i F_i}{f \sum_i c_i^2 w_i F_i}.$$

3.5.1.5.2 Back-Projection

Image reconstructions can also be calculated in real space. One of the methods is back-projection, which is the inverse of projection (Figure 3.6). While the projection compresses a 3D image into a 2D projection, back-projection smears out the 2D image information into the third dimension. The direction of back-projection is opposite to the direction of projection. To calculate an image reconstruction, the image information from different projections is back-projected into the direction of projection and averaged in the third dimension (Hoppe et al. 1986). Reconstructions by simple back-projection oversample the low-resolution information and thus generate reconstructions that are dominated by the low spatial frequencies. This is counteracted by weighting the image data with a weighting function that depends on the spatial frequency, the angular sampling, and the size of the reconstructed object (for more details, see Penczek 2010). Fourier inversion and back-projection are equivalent methods for reconstructing the 3D volume of the object. Some of the equivalent aspects are summarized in Table 3.2.

3.5.1.5.3 Postprocessing of the Three-Dimensional Map

In the reconstructed map, the signal at higher spatial frequencies is often underestimated due to the modulation transfer function of the detector, the spherical and chromatic aberrations of the electron microscope, uncertainties in the determination of the orientations of the particles, and conformational flexibility of the particles. These factors lead to a fast decay of high-resolution information. Therefore, for a realistic representation of the map, the signal at higher spatial frequencies has to be adjusted. One way forward is to measure small angle x-ray scattering curves of the particle in solution and to use these scattering curves for scaling the amplitudes at different spatial frequencies (Thuman-Commike et al. 1999). Unfortunately, it is not always possible to obtain such experimental scattering curves. Alternatively, Guinier plots (natural logarithm of the average structure factor as a function of spatial frequency[2] $1/d^2$) can be used to estimate the decay of the signal (Rosenthal and Henderson 2003). This follows the assumption that in the absence of any decay, the structure factors at higher spatial frequencies ($>1/10$ Å^{-1}) depend mainly on the random distribution of atoms and change very little with the spatial frequencies. The decay can be estimated by determining the linear slope of the Guinier plot at these higher spatial frequencies. The slope is comparable to the B-factor in crystallography. Depending on the resolution of the final map, B-factors between 150 Å^2 for high-resolution
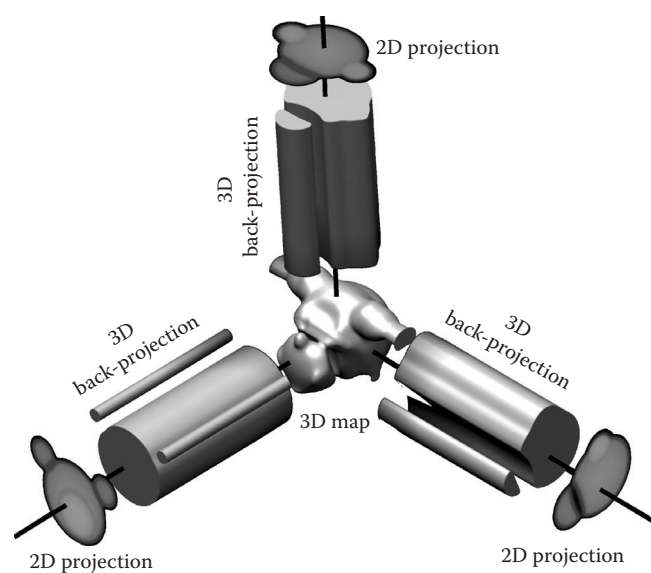

FIGURE 3.6 Image reconstruction in real space by back-projection. The object and its 2D projections are the same as shown in the example in Figure 3.5. The image is back-projected in the opposite direction as it was projected by expanding the gray values of the projection uniformly into the third dimension. The 3D back-projections of the different 2D projections are averaged in a single 3D map. A surface representation of the averaged back-projections is shown in the center of the map (3D map).

TABLE 3.2

Comparison of Image Reconstruction in Fourier Space and in Real Space

Real Space	Fourier Space
Conversion to Fourier space: Fourier transform	Conversion to real space: inverse Fourier transform
2D projection of image	Fourier transform of 2D projection
Back-projected 2D projection	Fourier transform of 2D projection as a section of the 3D Fourier transform
Diameter D of reconstructed object	Thickness of 2D section in the 3D Fourier transform of object: $1/D$
3D image reconstruction of object: back-projections of all image projections averaged in the third dimension	Fourier transform of 3D image reconstruction of object: Fourier transforms of all 2D projection added as sections in the 3D Fourier transform
Weighted back-projection of object (for review: Penczek 2010)	Averaging of Fourier sections with Fourier interpolation scheme (Grigorieff 2007)

EM maps (<4 Å) and 1000 Å^2 for intermediate-resolution EM maps (around 10 Å) have been reported. Subsequently, the signal at higher spatial frequencies in the maps is restored by applying a negative B-factor.

3.5.2 Image Processing of Unique Objects

For unique objects, all image information is obtained from a tilt series of the same object. Then, this tilt series is used for a tomographic reconstruction of the 3D map of the unique object. Similar to multicopy objects, the image processing of the tomograms consists of several steps that include preparing the images of the tilt series for further processing, aligning the different views of the tilt series to a common origin, determining the tilt angle and the orientation of the tilt axis, and finally reconstructing the 3D map of the object.

The considerations for preparing the raw data for further processing are similar as that for multicopy objects. In the preparation step, the images of the tilt series are cropped to the relevant area and to the same size. The gray value histograms of the individual images of the series are normalized and outliers such as very bright or very dark pixels are replaced by the average density of the surrounding pixels

In the next step, the images of the tilt series are aligned to a common origin and the orientation of the tilt axis and the tilt angle are calculated. The strategies for the alignment of the tilt series are somewhat different from the strategies used for multicopy objects: in principle, the common origin between the images of the tilt series could be determined by the cross-correlation between subsequent images of the tilt series, and the orientation of the tilt axis and the tilt angle are already known from the experimental setup. However, the accuracy with which these parameters are determined is insufficient for calculating high-resolution tomograms. The relative orientation of the images is more precisely determined by using fiducial markers. Such fiducials are colloidal gold particles, which can be easily identified in low-dose images (Fung et al. 1996; Diez et al. 2006) or landmarks in many small high-contrast patches of the image (Brandt et al. 2001; Castano-Diez et al. 2007; Sorzano et al. 2009). The exact position of the gold fiducials is determined by the density profile of the electron-dense marker, whereas the relative positions of the landmarks in patches are determined by cross-correlation. Then the tilt angle, the direction of the tilt axis, and the common origin of the micrographs of the series are determined by solving the transformation matrix and using the relative position of the same fiducials or landmarks in different images as input.

Subsequently, the tilt angle, the tilt axis, and the origin of the images of the tilt series are used to calculate the 3D image reconstruction, which is often done by weighted back-projection (see earlier text, multicopy objects). The image reconstruction is noisy due to the low dose of the individual images of the tilt series and the little overlap in information between subsequent images of the series. Furthermore, the limited tilt leads to missing information in the z-direction and thus an anisotropic representation of details in the reconstruction (Figure 3.7). Features

that are orientated perpendicular to the optical axis of the microscope are more accurately represented than features that have the same direction as the optical axis. For example, surface representations of tomograms of spherical virus particles often show details at the sides of the particle but are lacking the caps at the top and at the bottom (Figure 3.7).

3.5.2.1 Denoising of Tomograms

An important strategy for improving the representation of the image information is the denoising of the tomographic reconstructions. Many different techniques are available. Simple filters such as low-pass filter and block convolution are already quite efficient. In a low-pass filter, the higher spatial frequencies are attenuated, whereas low spatial frequencies are not affected. The filtration is done in Fourier space by multiplying the transform of the reconstruction with a filter function, which contains a spatial frequency-dependent weighting factor. The cutoff frequency for the filter is often chosen within the first transfer band of the CTF of the highest defocused image in the series. This avoids that information with the opposite contrast is included in the image reconstruction and thus makes correcting the image reconstruction for the CTF unnecessary. A filter function with a hard cutoff value in Fourier space introduces ripples at the edges of a high-contrast object in real space. Therefore, the edge of the filter function is typically smooth and gradually changes the weight over a larger frequency band, often with a Gaussian falloff. Generally, the low-pass filter suppresses high spatial frequencies, which are dominated by noise. Block convolution filters have a similar effect as low-pass filters but are computed in real space. In a block convolution, each pixel of the reconstruction is replaced by the average of the pixels in the surrounding subvolume. The size of the subvolume corresponds to the cutoff frequency in the low-pass filter.

Block convolution and low-pass filter only affect the transfer of the information, but they do not change the representation of the transmitted data. This is in contrast to filters that enhance certain features. Examples for such filters are median filters and anisotropic diffusion filters. Median filters work similarly as block convolution filters with the main difference that the pixel in the reconstruction is the median gray value of the surrounding subvolume instead of the average gray value. The median gray value is the value in the middle of the sorted series of gray values of the subvolume. Median filters are computationally more costly than block convolutions, but have the advantage that they enhance edges of features in the tomogram. The effect is further improved by applying the median filter several times iteratively to the tomogram (van der Heide et al. 2007). While edges are enhanced, features that are smaller than half of the box size of the median filter are potentially lost. Another approach for enhancing features in the tomogram is a nonlinear, anisotropic diffusion filter (Frangakis and Hegerl 1999, 2001; Fernandez and Li 2003). This type of filter takes the local gray value gradient into account and thus acts differently on noise and on signal of high- and low-contrast features. Therefore, details in the reconstruction are preserved and noise is efficiently repressed.
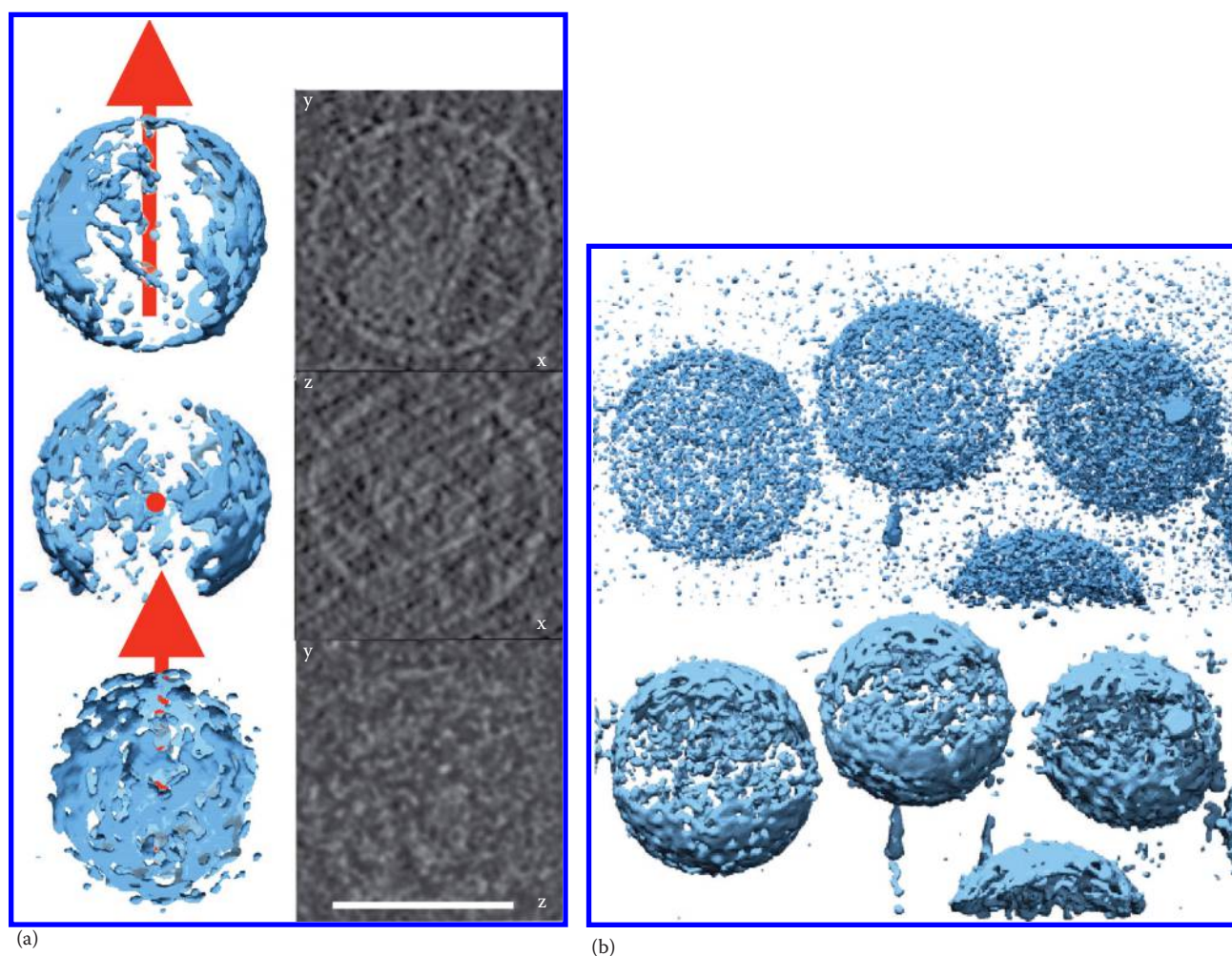
FIGURE 3.7 Tomogram of HIV virions (EMDB 1155, Briggs et al. 2006). (a) Left panels show surface representations of median filtered tomogram of a HIV virion; right panels show slices through the center of the tomogram of the virion in the same orientation as in the corresponding left panel. The position of the tilt axis is indicated in red in the surface representations, and the *x*, *y*, and *z* directions are labeled in the corresponding slices in the right panels. The length of the scale bar equals 100 nm. Different levels of detail are resolved in the tomogram, depending on the orientation relative to the tilt axis, demonstrating the effect of anisotropic resolution due to the limited tilt. (b) The top panel shows a surface representation of an unfiltered tomogram of several virions (EMDB 1155). The bottom panel shows a surface representation of the median filtered tomogram. Median filtering clearly reduces noise in the background and enhances the edges of the virions.

While simple filters such as block convolution and low-pass filter do not change the signal-to-noise in the transmitted resolution band, edge-enhancing filters do. Thus, edge-enhancing filters can increase the resolution somewhat. Denoising of tomograms is an essential step for improving the interpretability of the reconstructions and for calculating surface representations of a tomogram (Figure 3.7b).

3.5.2.2 Subtomogram Averaging

The resolution of a unique object in a tomogram is limited by noise. Currently, there are no strategies to overcome this limitation. However, unique objects often contain repeating building blocks, which can be regarded as multicopy objects within the unique object. Examples for such multicopy objects in polymorphic viral nanoparticles are virus surface glycoproteins (Liu et al. 2008b; Huiskonen et al. 2010; Tran et al. 2012; Maurer et al. 2013) and internal structural virus

proteins (de Marco et al. 2010; Bharat et al. 2011; Liljeroos et al. 2011; Schur et al. 2013), which both have been studied by subtomogram averaging.

Subtomogram averaging involves similar steps as image processing of isolated multicopy objects with the exception that the data do not consist of individual projections of the multicopy object but of 3D volumes with anisotropic resolution (due to the limited tilt of the tomogram). The workflow for subtomogram averaging consists of the identification of the multicopy object within the tomogram either by identifying the multicopy objects manually or by cross-correlating the tomogram with a template in different orientations. The highest cross-correlation peaks between the tomogram and the template are the likely positions of the multicopy objects within the tomogram. Often additional prior knowledge about the likely position of the object in the tomogram is incorporated for selecting the cross-correlation peaks. For example,

if the multicopy object is membrane bound or is located in a certain layer of the capsid, cross-correlation peaks at other places in the tomogram are ignored.

After the positions of the objects in the tomogram have been identified, small subvolumes of equal size are cut out. Ideally, the subvolumes contain one copy of the object each. In the next step, the subvolumes are aligned rotationally and translationally to a common reference volume. For the alignment, the missing wedge of the tomogram is taken into account and cross-correlation is restricted to information that is present in the reference and in the subvolume. Finally, aligned subvolumes are averaged and the whole process of alignment and averaging is repeated with the averaged subvolume as new reference. Often the template-based identification of the multicopy objects in the tomogram is also included in the iterative refinement process, because the accuracy of the localization of the multicopy objects within the tomogram improves with the improving template map.

The average of many aligned copies of a randomly orientated object has isotropic resolution, which is in contrast to the tomogram of the unique object. Furthermore, much higher resolution can be obtained in the subtomogram average, because the information of many objects is averaged. Thus, by averaging, the signal-to-noise ratio can be improved beyond the limit that is dictated by the tolerable dose of the unique object. It has been demonstrated that subnanometer resolution is achievable by subtomogram averaging of some 700,000 copies (Schur et al. 2013) (Figure 3.8).

The processing of subtomograms does not only give structural information of the multicopy object but it also informs where a certain multicopy object is located within a unique object and what its spatial relation to other objects is. This information gives important biological insights into the structural building principles of polymorphic particles.

3.6 EXAMPLES OF ELECTRON CRYOMICROSCOPY OF VIRAL NANOPARTICLES

Over the past 30 years, countless structural studies by electron cryomicroscopy and image processing of diverse viral nanoparticles have been published. These studies covered a wide range of aspects including structure determination of highly symmetrical icosahedral and helical virus particles and determining systematic breaks of their symmetry. These studies gave insights into the structural maturation of viral capsids and the packaging of the genome as well as of its delivery to the host.

3.6.1 HIGH-RESOLUTION STRUCTURAL STUDIES OF ICOSAHEDRAL NANOPARTICLES

For regular icosahedral nanoparticles, electron cryomicroscopy and image processing has emerged as an important alternative to crystallographic studies. The strength of electron cryomicroscopy is that the nanoparticles are studied under almost physiological buffer conditions unhindered by crystal contacts. Until the end of 2013, some 42 structures of viral nanoparticles or viral proteins with resolutions between 3.1 and 5 Å (Table 3.3) have been deposited in the EMDB, which is the unified repository for EM

(a)   Real-space helical reconstruction   (b)   Subtomogram averaging
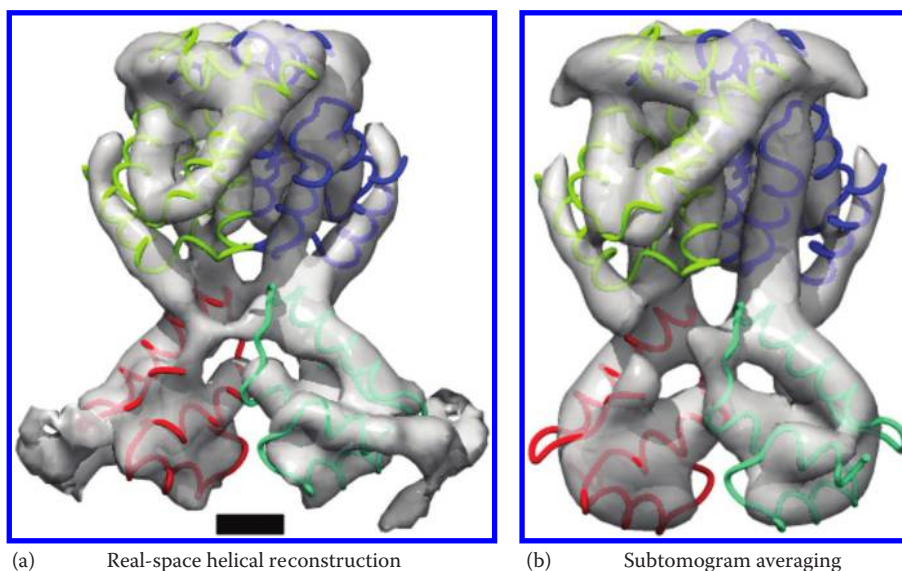
FIGURE 3.8   Surface representations of Mason-Pfizer Monkey virus capsid domain of Gag protein at 7–8 Å resolution with fitted model of the C-terminal (red and green) and N-terminal (yellow and blue) part of the capsid domain (4ARD, Bharat et al. 2012). (a) Real-space reconstruction of the helical assemblies followed by averaging of the independent copies in the asymmetric unit (EMD 2090, Bharat et al. 2012). Averaging of 344,000 units gave a resolution of 6.8 Å. (b) Subtomogram averaging of the capsid domain of the helical tubes. Averaging of 728,000 units gave a resolution of 8.3 Å (EMD 2488, Schur et al. 2013). Both reconstructions show a similar level of detail indicating that subtomogram averaging can deliver subnanometer resolution maps with similar reliability as conventional processing of multicopy objects. The length of the scale bar equals 1 nm.

TABLE 3.3

Maps of Viral Nanoparticles with 3–5 Å Resolution, Which Have Been Deposited in the EMDB until the End of 2013

Virus	EMDB Entry	Publication Year	Resolution	Microscope	Voltage (kV)	Detector	Averaged Number of Particles/Units	Remarks	Citations
Adeno-associated virus	EMD-5681	2013	4.8 Å	FEI Titan Krios	120	Gatan Ultrascan 4k × 4k CCD camera	70,725 particles/4.2 Mio units	Localization of sucrose octa sulfate in difference maps.	Xie et al. (2013)
Adeno-associated virus	EMD-5415	2012	4.5 Å	FEI Titan Krios	120	Gatan Ultrascan 4k × 4k CCD camera	27,312 particles/1.6 Mio units	Localization of an engineered loop. Structural differences to other serotypes might explain the different tropism of the engineered virus.	Lerch et al. (2012)
Cytoplasmic polyhedrosis virus: Bombyx mori cypovirus 1	EMD-1508	2008	3.9 Å	FEI Polara	300	TVIPS 4k × 4k CCD camera	12,814 particles/768,840 units	The structure of the whole virus was built de novo with O.	Yu et al. (2008)
Cytoplasmic polyhedrosis virus: Bombyx mori cypovirus	EMD-5233	2011	3.9 Å	FEI Titan Krios	300	Gatan Ultrascan 4k × 4k CCD camera	29,000 particles/1.7 Mio units		Cheng et al. (2011)
Cytoplasmic polyhedrosis virus: Bombyx mori cypovirus	EMD-5256	2011	3.1 Å	FEI Titan Krios	300	Film Kodak SO169	28,993 particles/1.7 Mio units	This 3.1 Å resolution map–enabled building of atomic models for all the structural proteins of CPV.	Yu et al. (2011)
Cytoplasmic polyhedrosis virus: Bombyx mori cypovirus	EMD-5376	2012	4.1 Å	FEI Titan Krios	300	Gatan Ultrascan 4k × 4k CCD camera	8,000 particles/480,000 units	The map reveals small-scale structural changes in the capsid that only occur in the transcribing virus.	Yang et al. (2012)
Sulfolobus turreted Icosahedral virus	EMD-5584	2013	4.5 Å	FEI Titan Krios	300	FEI Falcon I Direct detector	8,903 particles/534,180 units	The map reveals the structure of the whole virus and allows model building of the Cα trace.	Veesler et al. (2013)
Penicillium chrysogenum virus	EMD-5600	To be published	4.1 Å	FEI Tecnai F30	300				Luque et al. (2014)
Aquareovirus capsid proteins: Grass carp reovirus	EMD-1653	2010	4.5 Å	FEI Polara	300	TVIPS 4k × 4k CCD camera	15,000 particles/900,000 units	The structural modeling is based on homology modeling and constraints by the EM map.	Cheng et al. (2010)

(Continued)

TABLE 3.3 (*Continued*)

Maps of Viral Nanoparticles with 3–5 Å Resolution, Which Have Been Deposited in the EMDB until the End of 2013

Virus	EMDB Entry	Publication Year	Resolution	Microscope	Voltage (kV)	Detector	Averaged Number of Particles/Units	Remarks	Citations
Prochlorococcus phage P-SSP7	EMD-1713	2010	4.6 Å	JEOL 3200FSC Energy filter	300	Film Kodak SO163	36,000 particles/2.2 Mio units	The processing of the data without imposed icosahedral symmetry shows the structure of the portal protein at one of the vertices at 9 Å resolution.	Liu et al. (2010b)
Enterobacteria phage P22	EMD-1824 EMD-1826	2011	3.8 and 4 Å	JEOL 3200FSC Energy filter Specimen temperature 4 K	300	Film Kodak SO163	23,400 particles/1.4 Mio units and 18,300 particles/1.1 Mio units	This study compares the structure of the empty procapsid (EMD 1824) with the structure of the infectious virus particle (EMD 1826) at 4 Å resolution. The study reveals the role of the scaffolding protein and shows that the capsid undergoes coordinated conformational changes upon transition from the procapsid into the mature virion.	Chen et al. (2011)
Bordetella phage BPP-1	EMD-5764 EMD-5765 EMD-5766	2013	3.5 Å	FEI Titan Krios	300	Film Kodak SO163	39,549 particles/2.4 Mio units	The map shows a noncircularly permuted Johnson fold topology of MCP.	Zhang et al. (2013)
Dengue virus serotype 1	EMD-2142	2013	4.2 Å for virus and 3.5 Å for averaged heterotetramer	FEI Titan Krios	300	Film Kodak SO163	32,569 particles/2 Mio units and 6 Mio averaged heterotetramers	Three heterotetramers in the asymmetric unit were averaged for improving the resolution of the heterotetramer.	Zhang et al. (2013)
Bovine adenovirus 3	EMD-2272 and EMD-2273	2013	4.5 and 4.5 Å	FEI Titan Krios	300				Cheng et al. (2014)
Human adenovirus type 5	EMD-5172	2010	3.6 Å	FEI Titan Krios	300	Film Kodak SO163	31,815 particles/1.9 Mio units	The map identifies the residues that are important for the interaction between the minor and major proteins. The residues were further validated by mutational studies, which showed a mutation-dependent modulation of the particle stability.	Liu et al. (2010a)
Human adenovirus type 5	EMD-5467	2012	4.2 Å	FEI Titan Krios	300	Gatan Ultrascan 4k × 4k CCD camera	21,000 particles/1.3 Mio units	The map resolves large parts of the fiber at a somewhat lower resolution than the capsid. The Ad5 capsid is pseudotyped with the Ad35 fiber. The map provides insights into the fiber–receptor interaction.	Cao et al. (2012)
Hepatitis B core protein	EMD-2278	2013	3.5 Å	FEI Titan Krios	300	Film Kodak SO163	8,093 particles/485,580 units	The map of the full-length protein Hepatitis B core antigen complements information from the crystal structure of the C-terminally truncated protein (Wynne et al. 1999). The C-terminal linker domain is differently orientated than in the previously published crystal structure.	Yu et al. (2013)
Pseudomonas phage phi6	EMD-2364	2013	4.4 Å	FEI Titan Krios	300	Film Kodak SO163	18,236 particles/1 Mio units	Comparison of the P1 capsid protein in the capsid (EM map) with the crystallized P1 pentamers reveals the likely conformational switch that drives capsid maturation.	Nemecek et al. (2013)

(*Continued*)

TABLE 3.3 (*Continued*)

Maps of Viral Nanoparticles with 3–5 Å Resolution, Which Have Been Deposited in the EMDB until the End of 2013

Virus	EMDB Entry	Publication Year	Resolution	Microscope	Voltage (kV)	Detector	Averaged Number of Particles/Units	Remarks	Citations
Dengue virus (mature)	EMD-5499 (partial map) EMD-5520 (full map)	2013	3.6 Å	FEI Titan Krios	300	Film Kodak SO163	9,288 particles/557,280 units	The map shows the mature virus. Comparison to other states gives insights into the pH-dependent maturation process of the capsid.	Zhang et al. (2013)
Dengue virus type 4	EMD-2485	2013	4.1 Å	FEI Titan Krios	300	FEI Falcon I direct detector	16,602 particles/1 Mio units	The comparison to structures of other dengue virus serotypes suggests differences in the surface charge distribution, which may explain the differences in the cellular receptor binding.	Kostyuchenko et al. (2014)
Bacteriophage epsilon 15	EMD-5003	2008	4.5 Å	JEOL 3000SFF 4.2 K	300	Film Kodak SO163	36,259 particles/2.1 Mio units	The complete backbone trace of the major capsid protein (gene product 7) was derived from this map.	Jiang et al. (2008)
Bacteriophage epsilon 15	EMD-5678	2013	4.5 Å	JEOL 3000SFF Energy filter	300	Film Kodak SO163	14,000 particles/840,000 units	The resolution and reliability of the maps was validated by comparing multiple independent datasets.	Baker et al. (2013)
Bovine Papilloma virus type 1	EMD-5155 and EMD-5156	2010	4.2 and 3.6 Å after sixfold averaging	FEI Tecnai F30	300	Film Kodak SO163	3,997 particles/239,820 units and 1.4 Mio quasiequivalent units	The structural data suggest a different mode of interaction between the 72 pentameric units in the icosahedral capsid than deduced from an earlier crystal structure (Modis et al. 2002).	Wolf et al. (2010)
Aquareovirus	EMD-5160	2010	3.3 Å	FEI Titan Krios	300	Film Kodak SO163	18,464 particles/1.1 Mio units	The map shows that autocleavage of the membrane protein is important for priming the virus for cell entry. The map shows enough detail to suggest that Lys84 and Glu76 may facilitate the autocleavage in a nucleophilic attack.	Zhang et al. (2010)
Rhesus rotavirus	EMD-5199	2011	3.8 Å	FEI Tecnai F30	300	Film Kodak SO163	4,187 particles/3.2 Mio quasiequivalent units (averaging of the 60 asymmetric units and the 13 quasiequivalent units in the asymmetric unit)	The maps show how the two subfragments of VP4 (VP8* and VP5*) retain their association after proteolytic cleavage in the infectious virion.	Settembre et al. (2011)
Bovine rotavirus	EMD-1461	2008	3.8 Å	FEI Tecnai F30	300	Film Kodak SO163	8,400 particles/6.5 Mio quasiequivalent units	The study was used as proof of concept and for methods development; the comparison of the EM map with the x-ray structure of rotavirus at a similar resolution shows similar clarity and level of detail.	Zhang et al. (2008)
Rotavirus VP6	EMD-1752	2010	3.5 Å	FEI Tecnai F30	300	Film Kodak SO163	7,000 particles (from Zhang et al. 2008)/5.5 Mio quasiequivalent units	Same data were used as in Zhang et al. (2008), but the data were processed with symmetry-adapted functions. The final map shows a clear improvement in resolution.	Estrozi and Navaza (2010)

(*Continued*)

TABLE 3.3 (*Continued*)

Maps of Viral Nanoparticles with 3–5 Å Resolution, Which Have Been Deposited in the EMDB until the End of 2013

| Virus	EMDB Entry	Publication Year	Resolution	Microscope	Voltage (kV)	Detector	Averaged Number of Particles/Units	Remarks	Citations
Rotavirus VP6	EMD-5487 and EMD-5488	2012	4.9 Å (no movie motion correction) and 4.4 Å (motion corrected)	FEI Tecnai F20	200	Direct Detector DE12 Movies	807 particles/630,000 quasiequivalent units	The study was used as test of performance for direct counting detectors. Furthermore, the advantage of movie processing over processing of single high-dose images was tested; processing of separate movie frames leads to better results.	Campbell et al. (2012)
Rotavirus VP6–VP7 complex	EMD-1609	2009	4.2 Å	FEI Tecnai F30	300	Film Kodak SO163	3,780 particles/2.9 Mio quasiequivalent units	The map was used to build the structure of VP7. The model shows the N-terminal arm, which is missing in the crystal structure (Aoki et al. 2009).	Chen et al. (2009)
Venezuelan equine encephalitis virus	EMD-5275 and EMD-5276	2011	4.8 and 4.4 Å	Jeol 3200FSC Energy filter	300	Gatan Ultrascan 4k × 4k CCD camera	37,000 particles/2.2 Mio units and 8.8 Mio quasiequivalent units	The map resolves features that were missing in the crystal structures of domains of alphavirus subunits. These features are implicated in the fusion, assembly, and budding processes of alphaviruses.	Zhang et al. (2011)
Sputnik virus	EMD-5495 and EMD-5496	2012	3.5 and 3.8 Å	FEI Titan Krios	300	Film Kodak SO163	12,000 particles/720,000 units and 12,000 particles/720,000 units	The structure could be solved, where x-ray crystallography was not feasible. Particles were imaged over thin carbon film.	Zhang et al. (2012)
Tobacco mosaic virus	EMD-1316	2007	4.4 Å	FEI Tecnai 30	200	Film Kodak SO163	135 particles/212,550 units	The map identified better ordered region at lower radii (res 88–109) than previous x-ray fiber diffraction studies (Namba et al. 1989); most likely the reconstruction shows a different stable state of the capsid, which might be relevant for assembly/disassembly.	Sachse et al. (2007)
Tobacco mosaic virus	EMD-1730	2010	4.6 Å	FEI Polara	300	Gatan Ultrascan 4k × 4k CCD camera	260,000 units	The study was done as a proof of principle that conventional CCD cameras are suitable for high-resolution structural studies. The map shows the same solution structure as reported by the other cryo-EM study (Sachse et al. 2007).	Clare and Orlova (2010)
Tobacco mosaic virus	EMD-5185	2011	3.3 Å	FEI Titan Krios	300	Film Kodak SO 163	43,000 helical segments 1.3 Mio units	This work demonstrates that helical reconstruction is possible to atomic resolution. The map shows TMV in its metastable calcium-free assembly state, which is distinctly different from the x-ray fiber diffraction map of TMV (Namba et al. 1989).	Ge and Zhou (2011)
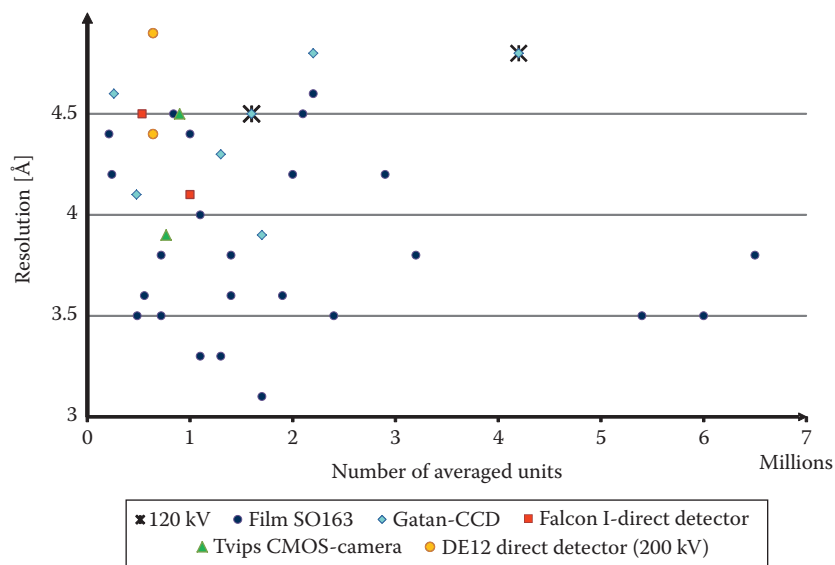
FIGURE 3.9 Plot of the resolution vs. the number of averaged units for maps of viral nanoparticles with 3–5 Å resolution taken with different types of detectors and at different accelerating voltages (see Table 3.3 for details). There is no strong dependency between the resolution and the number of averaged units in this resolution range. Maps with resolution better than 4 Å were predominantly recorded on film.

structures (Lawson et al. 2011). Analysis of the experimental conditions (Figure 3.9) highlights the important factors for achieving high resolution: Most of the structures have been obtained at an accelerating voltage of 300 kV, whereas only four structures have been determined from data recorded at lower voltages (two at 120 kV and two at 200 kV). All apart from one of the highest-resolution structures (<4 Å) were recorded on conventional film. Furthermore, the median number of units, which was averaged in a map with a resolution better than 5 Å, was 1.3 million, which is two to three orders of magnitude larger than what is expected if the only limiting factor would be the scattering efficiency of the object for electrons (Henderson 1995). In general, in the 3–5 Å resolution range, maps do not show a strong dependency of the resolution on the number of averaged units. This implies that other factors such as the structural heterogeneity of the particles, limitations in the imaging system, and beam-induced movement limit the resolution much more than the signal-to-noise ratio of the images. Interestingly, the four structures that have been determined with direct detectors (Falcon I or DE12) do not show any significant reduction in the number of averaged units, which are required for achieving a certain resolution compared to film or conventional CCD or CMOS detectors. This suggests that current image processing either cannot exploit the better signal transfer of the direct detectors at higher spatial frequencies or that the signal transfer of the detector is not the limiting factor. Probably, more studies will be needed to optimize the experimental conditions for the use of direct detectors to fully realize the potential of this new technology.

Maps derived from electron micrographs typically show very clear density with similar if not more detail than x-ray maps of the same object at the same resolution. Since electron microscopy starts to deliver more and more maps with comparable resolution as x-ray crystallography, it becomes important that resolution estimates in crystallography and electron microscopy give the same values for maps with similarly well-resolved features. The determination of the resolution in electron microscopy uses Fourier shell correlation between maps of two independent halves of the data for estimating the resolution (Harauz and Van Heel 1986). The Fourier shell correlation informs how well the halves agree at different spatial frequency and thus also give an estimate of the signal-to-noise ratio at these frequencies. For giving a single resolution value, a cutoff for the correlation (or signal-to-noise ratio) is required to determine the highest spatial frequency that still contains interpretable information. For a long time, there was a controversy which cutoff value is the *correct* one to use. Finally, Rosenthal and Henderson have shown that theoretically a Fourier shell correlation of 0.143 between maps of two independent halves of the noisy data (Rosenthal and Henderson 2003) equals a Fourier shell correlation of 0.5 (and thus a signal-to-noise ratio of 1) between a map of the combined image data and a noise-free reference map. Therefore, they suggested that a map with a resolution determined by a Fourier shell correlation cutoff of 0.143 between the two halves should have a similar quality as an x-ray map with the same resolution. Now that higher-resolution EM maps become available, this theoretical consideration can be tested and indeed the level of detail in EM maps and x-ray maps is most similar at the resolution given by the 0.143 cutoff criterion.

The higher-resolution EM maps contain sufficient information for building atomic models from scratch. They also show sufficient detail of the side chains to understand molecular switching mechanisms. An example for the quality of an EM density map together with the built-in structure
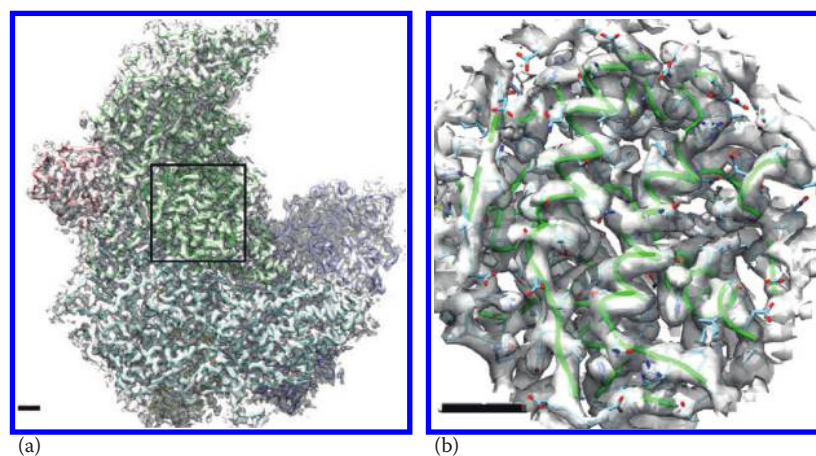
(a)   (b)

FIGURE 3.10 Model of the structural proteins VP1, VP3, and VP5 of Bombyx mori cypovirus capsid (3IXZ) built into the EM map (EMDB 5656) of the virus capsid at 3.1 Å resolution (Yu et al. 2011). (a) Two VP1 (green and cyan), one VP3 (blue) and two VP5 (red and yellow) proteins in the asymmetric unit together with the EM density map (gray). (b) A close-up of VP1 of the area indicated by a square in (a). The Cα backbone of the model is represented as a green ribbon diagram and the side chains are colored by element. The EM map shows distinct densities for the side chains of most residues. In both panels, the length of the scale bar equals 1 nm.

is shown in Figure 3.10 for the cytoplasmic polyhedrosis virus (Yu et al. 2011), which is the map with the highest resolution of a viral nanoparticle reported until the end of 2013. The map shows sufficient detail for ab initio building of the structures of all five proteins in the asymmetric unit. For the refinement of the model, CNS (*C*rystallography and *N*MR *S*ystem; Brunger et al. 1998; Brunger 2007) was used, which is a toolbox designed for model building in crystallography and NMR. To make the EM map accessible to the toolbox, pseudocrystallographic structure factors have been computed by arranging the EM density into a hypothetical crystal. With these pseudocrystallographic structure factors, standard crystallographic refinement procedures could be used for refining the atomic model against the map. Finally, the validity of the derived model was tested by calculating a free *R* factor, which is 27.3 for the model of the asymmetric unit of the cytoplasmic polyhedrosis virus against the EM map.

The somewhat lower-resolution structures (4–5 Å) of viral nanoparticles resolve the secondary structural elements but do not resolve all types of side chains. In many cases, the information of these maps is still sufficient for building Cα traces of the proteins from scratch. However, depending on the resolution of the map, building the Cα trace can be error prone. As an alternative to ab initio model building, homology models can be adapted to the observed density maps (Topf et al. 2008; Cheng et al. 2010; Zhu et al. 2010). The approach uses the cryo-EM map as additional constraint for the homology modeling and thus also allows modeling of conformational changes between the observed structure and the known structure of a homologue. The method is based on molecular dynamics simulations of the model with the density map as a force field that drives the model into the EM map (Topf et al. 2008). For reducing the computational demand of the molecular dynamics simulations, the model refinement can be focused onto areas that do not fit well into

the observed EM map (Zhu et al. 2010). The method is very powerful and works similarly well with lower-resolution maps (resolution ≈ 7 Å) as constraints (Zhu et al. 2010). Therefore, structure-guided homology modeling is an emerging tool for modeling the structure of viral nanoparticles from EM maps at intermediate resolution.

3.6.2 Dealing with Asymmetric Attachments

Many icosahedral viral nanoparticles have single asymmetric attachments at one of their vertices like, for example, portal proteins that are essential for genome packaging and genome delivery to the host. To understand the function of these portal proteins in greater structural detail, it is necessary to investigate them in the context of the capsid. However, the information of the single portal overlaps with the image information of the icosahedrally ordered capsid that dominates the image information. Icosahedrally averaged capsids only show weak ghosts of the portal proteins at all vertices. Just relaxing the symmetry in the processing of the whole assembly is often not sufficient to determine the unique orientations of the capsids together with the portal at one of the vertices. To overcome this problem, one strategy is to generate an artificial reference, which contains one asymmetric attachment on a single vertex. Such a reference can be generated, by combining the symmetric reconstruction of the capsid with the reconstruction of an isolated attachment added to one of the vertices (Lander et al. 2006). In addition, the ghosts of the attachments at the other vertices are masked off to enhance the asymmetric contribution of the single attachment. This generates an artificial reference model of the whole assembly with the densities of the unique portal and of the capsid being at the same level. Such a reference is suitable for determining the unique orientations of the capsids with attached portal. This approach was quite successful for processing
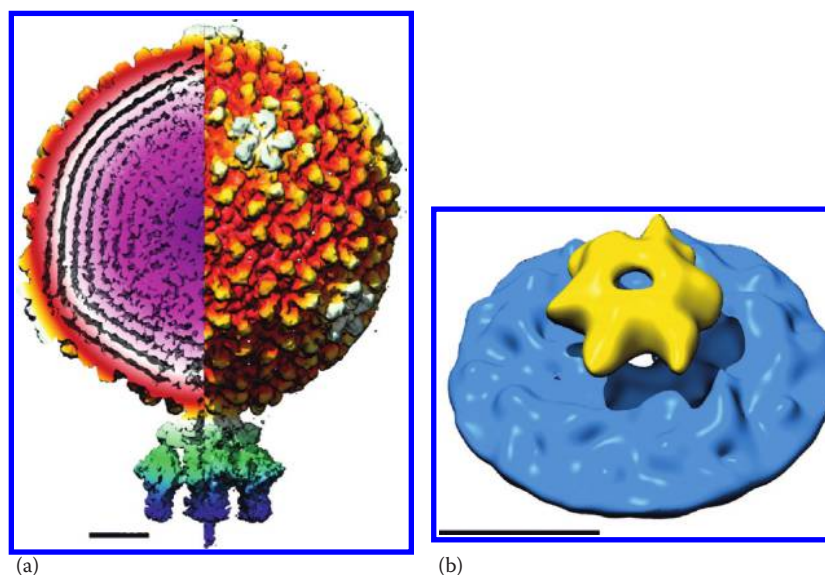
FIGURE 3.11 Reconstruction of asymmetric attachments to icosahedral viral nanoparticles: (a) Asymmetric reconstruction of P22 together with its portal protein (EMDB 5348, Tang et al. 2011). The surface is colored according to the radial distance from the center of the capsid. (b) Vertex reconstruction of the hexameric RNA packaging motor in a viral polymerase complex (EMDB 1256, Huiskonen et al. 2007). The hexagonal RNA packaging motor is shown in yellow, and the icosahedral RNA polymerase complex of cystovirus Φ8 is shown in blue. The length of the scale bars equals 10 nm.

bacteriophages such as P22 (Tang et al. 2011) for which the capsid together with its portal protein could be resolved at subnanometer resolution (Figure 3.11a).

For smaller attachments or attachments at several sides of the icosahedral nanoparticle, it is more difficult to identify the position and the structure of the asymmetric contribution. For these assemblies, an alternative approach has been proposed, which aims at only reconstructing the asymmetric attachment at a vertex of the capsid (Briggs et al. 2005). In these vertex reconstructions, the capsids are first processed, assuming full icosahedral symmetry. Then the orientational information of the capsid is used to identify the positions of the vertices. The vertices are extracted and their image information is classified to discern between vertices with and without attachments. For the vertices with attachment, the position and the out-of-plane tilt of the attachment is already known from the capsid orientation. So, the only parameter that is still missing is the relative rotation of the attachment around the vertex axis, which can be determined by angular reconstitution (Schatz et al. 1997). An example is shown for the hexameric packaging motor (about 200 kDa), which is attached to the fivefold vertex of the icosahedral polymerase complex (about 33 MDa) of cystovirus Φ8 (Huiskonen et al. 2007) in Figure 3.11b. Here, a very small attachment can be correctly reconstructed without disturbance by the some 150 times larger icosahedral carrier.

REFERENCES

Adrian, M., J. Dubochet et al. (1984). Cryo-electron microscopy of viruses. *Nature* **308**(5954): 32–36.

Angert, I., E. Majorovits et al. (2000). Zero-loss image formation and modified contrast transfer theory in EFTEM. *Ultramicroscopy* **81**(3–4): 203–222.

Aoki, S. T., E. C. Settembre et al. (2009). Structure of rotavirus outer-layer protein VP7 bound with a neutralizing Fab. *Science* **324**(5933): 1444–1447.

Bai, X. C., I. S. Fernandez et al. (2013). Ribosome structures to near-atomic resolution from thirty thousand cryo-EM particles. *Elife* **2**: e00461.

Baker, L. A., E. A. Smith et al. (2010). The resolution dependence of optimal exposures in liquid nitrogen temperature electron cryomicroscopy of catalase crystals. *J Struct Biol* **169**(3): 431–437.

Baker, M. L., C. F. Hryc et al. (2013). Validated near-atomic resolution structure of bacteriophage epsilon15 derived from cryo-EM and modeling. *Proc Natl Acad Sci USA* **110**(30): 12301–12306.

Baker, T. S., N. H. Olson et al. (1999). Adding the third dimension to virus life cycles: Three-dimensional reconstruction of icosahedral viruses from cryo-electron micrographs. *Microbiol Mol Biol Rev* **63**(4): 862–922, table of contents.

Baschong, W., U. Aebi et al. (1988). Head structure of bacteriophages T2 and T4. *J Ultrastruct Mol Struct Res* **99**(3): 189–202.

Baumeister, W. and J. Seredynski (1976). Preparation of perforated films with pre-determinable hole size distributions. *Micron* **7**(1): 49–54.

Bayer, M. E. and T. F. Anderson (1963). Preparation of holey films for electron microscopy. *Experientia* **19**(8): 433–434.

Bellare, J. R., H. T. Davis et al. (1988). Controlled environment vitrification system: An improved sample preparation technique. *J Electron Microsc Tech* **10**: 87–111.

Berriman, J. and N. Unwin (1994). Analysis of transient structures by cryo-microscopy combined with rapid mixing of spray droplets. *Ultramicroscopy* **56**: 241–252.

Bharat, T. A., N. E. Davey et al. (2012). Structure of the immature retroviral capsid at 8 Å resolution by cryo-electron microscopy. *Nature* **487**(7407): 385–389.

Bharat, T. A., J. D. Riches et al. (2011). Cryo-electron tomography of Marburg virus particles and their morphogenesis within infected cells. *PLoS Biol* **9**(11): e1001196.

Booy, F. P. and J. B. Pawley (1993). Cryo-crinkling: What happens to carbon films on copper grids at low temperature. *Ultramicroscopy* **48**(3): 273–280.

Böttcher, B. and R. A. Crowther (1996). Difference imaging reveals ordered regions of RNA in turnip yellow mosaic virus. *Structure* **4**(4): 387–394.

Böttcher, B., S. A. Wynne et al. (1997). Determination of the fold of the core protein of hepatitis B virus by electron cryomicroscopy. *Nature* **386**(6620): 88–91.

Brandt, S., J. Heikkonen et al. (2001). Automatic alignment of transmission electron microscope tilt series without fiducial markers. *J Struct Biol* **136**(3): 201–213.

Brenner, S. and R. W. Horne (1959). A negative staining method for high resolution electron microscopy of viruses. *Biochim Biophys Acta* **34**: 103–110.

Briggs, J. A., K. Grunewald et al. (2006). The mechanism of HIV-1 core assembly: Insights from three-dimensional reconstructions of authentic virions. *Structure* **14**(1): 15–20.

Briggs, J. A., J. T. Huiskonen et al. (2005). Classification and three-dimensional reconstruction of unevenly distributed or symmetry mismatched features of icosahedral particles. *J Struct Biol* **150**(3): 332–339.

Brilot, A. F., J. Z. Chen et al. (2012). Beam-induced motion of vitrified specimen on holey carbon film. *J Struct Biol* **177**(3): 630–637.

Bruggeller, P. and E. Mayer (1980). Complete vitrification in pure liquid water and dilute aqueous-solutions. *Nature* **288**(5791): 569–571.

Brunger, A. T. (2007). Version 1.2 of the crystallography and NMR system. *Nat Protoc* **2**(11): 2728–2733.

Brunger, A. T., P. D. Adams et al. (1998). Crystallography & NMR system: A new software suite for macromolecular structure determination. *Acta Crystallogr D Biol Crystallogr* **54**(Pt 5): 905–921.

Campbell, M. G., A. Cheng et al. (2012). Movies of ice-embedded particles enhance resolution in electron cryo-microscopy. *Structure* **20**(11): 1823–1828.

Cao, C., X. Dong et al. (2012). Conserved fiber-penton base interaction revealed by nearly atomic resolution cryo-electron microscopy of the structure of adenovirus provides insight into receptor interaction. *J Virol* **86**(22): 12322–12329.

Castano-Diez, D., A. Al-Amoudi et al. (2007). Fiducial-less alignment of cryo-sections. *J Struct Biol* **159**(3): 413–423.

Chen, D. H., M. L. Baker et al. (2011). Structural basis for scaffolding-mediated assembly and maturation of a dsDNA virus. *Proc Natl Acad Sci USA* **108**(4): 1355–1360.

Chen, J. Z., C. Sachse et al. (2008). A dose-rate effect in single-particle electron microscopy. *J Struct Biol* **161**(1): 92–100.

Chen, J. Z., E. C. Settembre et al. (2009). Molecular interactions in rotavirus assembly and uncoating seen by high-resolution cryo-EM. *Proc Natl Acad Sci USA* **106**(26): 10644–10648.

Cheng, L., X. Huang et al. (2014). Cryo-EM structures of two bovine adenovirus type 3 intermediates. *Virology* **450**: 174–181.

Cheng, L., J. Sun et al. (2011). Atomic model of a cypovirus built from cryo-EM structure provides insight into the mechanism of mRNA capping. *Proc Natl Acad Sci USA* **108**(4): 1373–1378.

Cheng, L., J. Zhu et al. (2010). Backbone model of an aquareovirus virion by cryo-electron microscopy and bioinformatics. *J Mol Biol* **397**(3): 852–863.

Chester, D. W., J. F. Klemic et al. (2007). Holey carbon micro-arrays for transmission electron microscopy: A microcontact printing approach. *Ultramicroscopy* **107**(8): 685–691.

Clare, D. K. and E. V. Orlova (2010). 4.6Å Cryo-EM reconstruction of tobacco mosaic virus from images recorded at 300 keV on a 4k × 4k CCD camera. *J Struct Biol* **171**(3): 303–308.

Conway, J. F., N. Chenng et al. (1997). Visualization of a4-helix bundle in the hepatitis B virus capsid by cryo-electron microscopy. *Nature* **368**(6): 91–94.

Conway, J. F., B. L. Trus et al. (1993). The effects of radiation damage on the structure of frozen hydrated HSV-1 capsids. *J Struct Biol* **111**: 222–233.

Crowther, R. A. (1971). Procedures for three-dimensional reconstruction of spherical viruses by Fourier synthesis from electron micrographs. *Phil Trans R Soc* **261**: 221–230.

Crowther, R. A., L. A. Amos et al. (1970a). Three dimensional reconstructions of spherical viruses by Fourier synthesis from electron micrographs. *Nature* **226**(244): 421–425.

Crowther, R. A., D. J. DeRosier et al. (1970b). The reconstruction of a three-dimensional structure from projections and its application to electron microscopy. *Proc R Soc Lond A* **A317**: 319–340.

Crowther, R. A., N. A. Kiselev et al. (1994). Three-dimensional structure of Hepatitis B virus core particles determined by electron cryomicroscopy. *Cell* **77**: 943–950.

Cyrklaff, M., M. Adrian et al. (1990). Evaporation during preparation of unsupported thin vitrified aqueous layers for cryo-electron microscopy. *J Electron Microsc Tech* **16**(4): 351–355.

Danev, R., S. Kanamaru et al. (2010). Zernike phase contrast cryo-electron tomography. *J Struct Biol* **171**(2): 174–181.

de Marco, A., B. Muller et al. (2010). Structural analysis of HIV-1 maturation using cryo-electron tomography. *PLoS Pathog* **6**(11): e1001215.

DeRosier, D. J. and A. Klug (1968). Reconstruction of three dimensional structures from electron micrographs. *Nature* **217**: 130–134.

Diez, D. C., A. Seybert et al. (2006). Tilt-series and electron microscope alignment for the correction of the non-perpendicularity of beam and tilt-axis. *J Struct Biol* **154**(2): 195–205.

Dubochet, J. (2012). Cryo-EM—The first thirty years. *J Microsc* **245**(3): 221–224.

Dubochet, J., M. Adrian et al. (1988). Cryo-electron microscopy of vitrified specimens. *Q Rev Biophys* **21**(2): 129–228.

Dubochet, J., M. Adrian et al. (1994). Structure of intracellular mature vaccinia virus observed by cryoelectron microscopy. *J Virol* **68**(3): 1935–1941.

Dubochet, J., M. Ducommun et al. (1971). A new preparation method for dark-field electron microscopy of biomacromolecules. *J Ultrastruct Res* **35**(1): 147–167.

Dubochet, J., J. Lepault et al. (1982). Electron microscopy of frozen water and aqueous solutions. *J Microsc* **128**: 219–237.

Dubochet, J. and A. McDowall (1981). Vitrification of pure water for electron microscopy. *J Microsc* **124**: 3–4.

Dubochet, J., A. W. McDowall et al. (1983). Electron microscopy of frozen-hydrated bacteria. *J Bacteriol* **155**(1): 381–390.

Egelman, E. H. (2000). A robust algorithm for the reconstruction of helical filaments using single-particle methods. *Ultramicroscopy* **85**(4): 225–234.

Egelman, E. H. (2010). Reconstruction of helical filaments and tubes. *Methods Enzymol* **482**:167–183.

Ermantraut, E., K. Wohlfahrt et al. (1998). Perforated support foils with pre-defined hole size, shape and arrangement. *Ultramicroscopy* **74**: 75–81.

Estrozi, L. F. and J. Navaza (2010). Ab initio high-resolution single-particle 3D reconstructions: The symmetry adapted functions way. *J Struct Biol* **172**(3): 253–260.

Fan, G. Y., S. J. Young et al. (1995). Conditions for electron tomographic data acquisition. *J Electron Microsc* (*Tokyo*) **44**(1): 15–21.

Fernandez, J. J. and S. Li (2003). An improved algorithm for anisotropic nonlinear diffusion for denoising cryo-tomograms. *J Struct Biol* **144**(1–2): 152–161.

Frangakis, A. S. and R. Hegerl (1999). Nonlinear anisotropic diffusion in three-dimensional electron microscopy. *Scale-Space Theor Comput Vis* **1682**: 386–397.

Frangakis, A. S. and R. Hegerl (2001). Noise reduction in electron tomographic reconstructions using nonlinear anisotropic diffusion. *J Struct Biol* **135**(3): 239–250.

Franklin, R. E. and K. C. Holmes (1958). Tobacco mosaic virus—Application of the method of isomorphous replacement to the determination of the helical parameters and radial density distribution. *Acta Crystallogr* **11**(3): 213–220.

Frederik, P. M. and D. H. W. Hubert (2005). Cryoelectron microscopy of liposomes. *Methods Enzymol* **391**: 431–448.

Fung, J. C., W. Liu et al. (1996). Toward fully automated high-resolution electron tomography. *J Struct Biol* **116**(1): 181–189.

Ge, P. and Z. H. Zhou (2011). Hydrogen-bonding networks and RNA bases revealed by cryo electron microscopy suggest a triggering mechanism for calcium switches. *Proc Natl Acad Sci USA* **108**(23): 9637–9642.

Glaeser, R. M., D. Typke et al. (2011). Precise beam-tilt alignment and collimation are required to minimize the phase error associated with coma in high-resolution cryo-EM. *J Struct Biol* **174**(1): 1–10.

Grigorieff, N. (2007). FREALIGN: High-resolution refinement of single particle structures. *J Struct Biol* **157**(1): 117–125.

Grimm, R., D. Typke et al. (1996). Determination of the inelastic mean free path in ice by examination of tilted vesicles and automated most probable loss imaging. *Ultramicroscopy* **63**(3–4): 169–179.

Harauz, G. and M. Van Heel (1986). Exact filters for general geometry 3-dimensional reconstruction. *Optik* **73**(4): 146–156.

Harris, W. J. (1962). Holey films for electron microscopy. *Nature* **196**(4853): 499–500.

Heide, H. G. (1984). Observation on ice layers. *Ultramicroscopy* **14**: 271–278.

Henderson, R. (1995). The potential and limitations of neutrons, electrons and X-rays for atomic resolution microscopy of unstained biological molecules. *Q Rev Biophys* **28**(2): 171–193.

Henderson, R. (2004). Realizing the potential of electron cryomicroscopy. *Q Rev Biophys* **37**: 3–13.

Henrick, K., R. Newman et al. (2003). EMDep: A web-based system for the deposition and validation of high-resolution electron microscopy macromolecular structural information. *J Struct Biol* **144**(1–2): 228–237.

Hoppe, W., H. J. Schramm et al. (1986). Three-dimensional electron microscopy of individual biological objects. *Z Naturforsch A* **31**: 645–655.

Huiskonen, J. T., J. Hepojoki et al. (2010). Electron cryotomography of Tula hantavirus suggests a unique assembly paradigm for enveloped viruses. *J Virol* **84**(10): 4889–4897.

Huiskonen, J. T., H. T. Jaalinoja et al. (2007). Structure of a hexameric RNA packaging motor in a viral polymerase complex. *J Struct Biol* **158**(2): 156–164.

Jager, J. (1990). Herstellung von freitragenden Eisfilmen auf Kupfernetzchen zur Einbettung biologischer Makromolekule fur die EM-Beobachtung. *Elektronenmikroskopie* **1**: 24–28.

Jiang, W., M. L. Baker et al. (2008). Backbone structure of the infectious epsilon15 virus capsid revealed by electron cryomicroscopy. *Nature* **451**(7182): 1130–1134.

Johnson, R. P. and D. W. Gregory (1993). Viruses accumulate spontaneously near droplet surfaces: A method to concentrate viruses for electron microscopy. *J Microsc* **171**: 125–136.

Kausche, G. A., E. Pfankuch et al. (1939). The visualisation of herbal viruses in surface microscopes. *Naturwissenschaften* **27**: 292–299.

Kelly, D. F., P. D. Abeyrathne et al. (2008). The affinity grid: A prefabricated EM grid for monolayer purification. *J Mol Biol* **382**(2): 423–433.

Kelly, D. F., D. Dukovski et al. (2010). A practical guide to the use of monolayer purification and affinity grids. *Methods Enzymol* **481**(*Cryo-Em, Part A—Sample Preparation and Data Collection*): 83–107.

Klug, A. and J. E. Berger (1964). An optical method for the analysis of periodicities in electron micrographs, and some observations on the mechanism of negative staining. *J Mol Biol* **10**: 565–569.

Klug, A. and D. L. Caspar (1960). The structure of small viruses. *Adv Virus Res* **7**: 225–325.

Klug, A. and D. J. DeRosier (1966). Optical filtering of electron micrographs: Reconstruction of one-sided images. *Nature* **212**: 29–32.

Korinek, A., F. Beck et al. (2011). Computer controlled cryo-electron microscopy—TOM(2) a software package for high-throughput applications. *J Struct Biol* **175**(3): 394–405.

Kostyuchenko, V. A., P. L. Chew et al. (2014). Near-atomic resolution cryo-electron microscopic structure of dengue serotype 4 virus. *J Virol* **88**(1): 477–482.

Kourkoutis, L. F., J. M. Plitzko et al. (2012). Electron microscopy of biological materials at the nanometer scale. *Annu Rev Mater Res* **42**: 33–58.

Krimm, S. and T. F. Anderson (1967). Structure of normal and contracted tail sheaths of T4 bacteriophage. *J Mol Biol* **27**(2): 197–202.

Kronenberg, S., J. A. Kleinschmidt et al. (2001). Electron cryomicroscopy and image reconstruction of adeno-associated virus type 2 empty capsids. *EMBO Rep* **2**(11): 997–1002.

Kutsay, O., O. Loginova et al. (2008). Surface properties of amorphous carbon films. *Diamond Relat Mater* **17**(7–10): 1689–1691.

Lander, G. C., L. Tang et al. (2006). The structure of an infectious P22 virion shows the signal for headful DNA packaging. *Science* **312**(5781): 1791–1795.

Lawson, C. L., M. L. Baker et al. (2011). EMDataBank.org: Unified data resource for CryoEM. *Nucleic Acids Res* **39**(Database issue): D456–D464.

Lei, J. and J. Frank (2005). Automated acquisition of cryo-electron micrographs for single particle reconstruction on an FEI Tecnai electron microscope. *J Struct Biol* **150**(1): 69–80.

Lepault, J., F. P. Booy et al. (1983). Electron microscopy of frozen biological suspensions. *J Microsc* **129**(Pt 1): 89–102.

Lepault, J. and J. Dubochet (1986). Electron microscopy of frozen hydrated specimens: Preparation and characteristics. *Methods Enzymol* **127**: 719–730.

Lerch, T. F., J. K. O'Donnell et al. (2012). Structure of AAV-DJ, a retargeted gene therapy vector: Cryo-electron microscopy at 4.5 Å resolution. *Structure* **20**(8): 1310–1320.

Li, X., P. Mooney et al. (2013). Electron counting and beam-induced motion correction enable near-atomic-resolution single-particle cryo-EM. *Nat Methods* **10**(6): 584–590.

Liljeroos, L., J. T. Huiskonen et al. (2011). Electron cryotomography of measles virus reveals how matrix protein coats the ribonucleocapsid within intact virions. *Proc Natl Acad Sci USA* **108**(44): 18085–18090.

Liu, H., L. Cheng et al. (2008a). Symmetry-adapted spherical harmonics method for high-resolution 3D single-particle reconstructions. *J Struct Biol* **161**(1): 64–73.

Liu, H., L. Jin et al. (2010a). Atomic structure of human adenovirus by cryo-EM reveals interactions among protein networks. *Science* **329**(5995): 1038–1043.

Liu, J., A. Bartesaghi et al. (2008b). Molecular architecture of native HIV-1 gp120 trimers. *Nature* **455**(7209): 109–113.

Liu, X., Q. Zhang et al. (2010b). Structural changes in a marine podovirus associated with release of its genome into *Prochlorococcus*. *Nat Struct Mol Biol* **17**(7): 830–836.

Liu, Z. F., L. H. Jiang et al. (2010c). A graphene oxide center dot streptavidin complex for biorecognition—Towards affinity purification. *Adv Funct Mater* **20**(17): 2857–2865.

Lu, Z., T. R. Shaikh et al. (2009). Monolithic microfluidic mixing-spraying devices for time-resolved cryo-electron microscopy. *J Struct Biol* **168**(3): 388–395.

Luque, D., J. Gomez-Blanco et al. (2014). Cryo-EM near-atomic structure of a dsRNA fungal virus shows ancient structural motifs preserved in the dsRNA viral lineage. *Proc. Nat. Acad. Sci. USA* **111**: 7641–7646.

Maki-Yonekura, S., K. Yonekura et al. (2010). Conformational change of flagellin for polymorphic supercoiling of the flagellar filament. *Nat Struct Mol Biol* **17**(4): 417–422.

Markham, R., S. Frey et al. (1963). Methods for enhancement of image detail and accentuation of structure in electron microscopy. *Virology* **20**(1): 88–102.

Markham, R., G. J. Hills et al. (1964). Anatomy of tobacco mosaic virus. *Virology* **22**(3): 342–359.

Marko, M., A. Leith et al. (2011). Retrofit implementation of Zernike phase plate imaging for cryo-TEM. *J Struct Biol* **174**(2): 400–412.

Mastronarde, D. N. (2005). Automated electron microscope tomography using robust prediction of specimen movements. *J Struct Biol* **152**(1): 36–51.

Matricardi, V. R., R. C. Moretz et al. (1972). Electron diffraction of wet proteins: Catalase. *Science* **177**(45): 268–270.

Matthews, R. E. F., R. W. Horne et al. (1956). Electron microscope observations of periodicities in the surface structure of tobacco mosaic virus. *Nature* **178**(4534): 635–636.

Maurer, U. E., T. Zeev-Ben-Mordehai et al. (2013). The structure of herpesvirus fusion glycoprotein B-bilayer complex reveals the protein-membrane and lateral protein-protein interaction. *Structure* **21**(8): 1396–1405.

Mayer, E. and P. Bruggeller (1983). Devitrification of glassy water—Evidence for a discontinuity of state. *J Phys Chem* **87**(23): 4744–4749.

McClain, B., E. Settembre et al. (2010). X-ray crystal structure of the rotavirus inner capsid particle at 3.8 Å resolution. *J Mol Biol* **397**(2): 587–599.

McDowall, A. W., J. J. Chang et al. (1983). Electron microscopy of frozen hydrated sections of vitreous ice and vitrified biological samples. *J Microsc* **131**(Pt 1): 1–9.

McMullan, G., S. Chen et al. (2009a). Detective quantum efficiency of electron area detectors in electron microscopy. *Ultramicroscopy* **109**(9): 1126–1143.

McMullan, G., A. R. Faruqi et al. (2009b). Experimental observation of the improvement in MTF from backthinning a CMOS direct electron detector. *Ultramicroscopy* **109**(9): 1144–1147.

Mellema, J. E. and L. A. Amos (1972). Three-dimensional image reconstruction of turnip yellow mosaic virus. *J Mol Biol* **72**: 819–822.

Meyer, J. C., A. K. Geim et al. (2007). The structure of suspended graphene sheets. *Nature* **446**(7131): 60–63.

Mindell, J. A. and N. Grigorieff (2003). Accurate determination of local defocus and specimen tilt in electron microscopy. *J Struct Biol* **142**(3): 334–347.

Modis, Y., B. L. Trus et al. (2002). Atomic model of the papillomavirus capsid. *EMBO J* **21**(18): 4754–4762.

Moharir, A. V. and N. Prakash (1975). Formvar holey films and nets for electron-microscopy. *J Phys E—Sci Instrum* **8**(4): 288–290.

Murata, K., X. Liu et al. (2010). Zernike phase contrast cryo-electron microscopy and tomography for structure determination at nanometer and subnanometer resolutions. *Structure* **18**(8): 903–912.

Murray, J. M. and R. Ward (1987). Preparation of holey carbon films suitable for cryo-electron microscopy. *J Electron Microsc Tech* **5**: 285–290.

Namba, K., R. Pattanayek et al. (1989). Visualization of protein-nucleic acid interaction in a virus: Refined structure of intact tobacco mosaic virus at 2.9Å resolution by X-ray fiber diffraction. *J Mol Biol* **208**: 307–325.

Navaza, J. (2003). On the three-dimensional reconstruction of icosahedral particles. *J Struct Biol* **144**(1–2): 13–23.

Nemecek, D., E. Boura et al. (2013). Subunit folds and maturation pathway of a dsRNA virus capsid. *Structure* **21**(8): 1374–1383.

Nixon, H. L. and R. D. Woods (1960). The structure of tobacco mosaic virus protein. *Virology* **10**(1): 157–159.

Novoselov, K. S., A. K. Geim et al. (2004). Electric field effect in atomically thin carbon films. *Science* **306**(5696): 666–669.

Olson, N. H., P. R. Kolatkar et al. (1993). Structure of human rhinovirus complexed with its receptor molecule. *Proc Natl Acad Sci USA* **90**: 507–511.

Pantelic, R. S., J. C. Meyer et al. (2012). The application of graphene as a sample support in transmission electron microscopy. *Solid State Commun* **152**(15): 1375–1382.

Pantelic, R. S., J. W. Suk et al. (2011). Graphene: Substrate preparation and introduction. *J Struct Biol* **174**(1): 234–238.

Penczek, P. A. (2010). Fundamentals of three-dimensional reconstruction from projections. *Methods Enzymol* **482**: 1–33.

Quispe, J., J. Damiano et al. (2007). An improved holey carbon film for cryo-electron microscopy. *Microsc Microanal* **13**(5): 365–371.

Rosenthal, P. B. and R. Henderson (2003). Optimal determination of particle orientation, absolute hand, and contrast loss in single-particle electron cryomicroscopy. *J Mol Biol* **333**(4): 721–745.

Ruskin, R. S., Z. Yu et al. (2013). Quantitative characterization of electron detectors for transmission electron microscopy. *J Struct Biol* **184**(3): 385–393.

Sachse, C., J. Z. Chen et al. (2007). High-resolution electron microscopy of helical specimens: A fresh look at tobacco mosaic virus. *J Mol Biol* **371**(3): 812–835.

Schatz, M., E. V. Orlova et al. (1995). Structure of *Lumbricus terrestris* hemoglobin at 30 Å resolution determined using angular reconstitution. *J Struct Biol* **114**(1): 28–40.

Schatz, M., E. V. Orlova et al. (1997). Angular reconstitution in three-dimensional electron microscopy: Practical and technical aspects. *Scan Microsc* **11**: 179–193.

Schur, F. K., W. J. Hagen et al. (2013). Determination of protein structure at 8.5Å resolution using cryo-electron tomography and sub-tomogram averaging. *J Struct Biol* **184**(3): 394–400.

Settembre, E. C., J. Z. Chen et al. (2011). Atomic model of an infectious rotavirus particle. *EMBO J* **30**(2): 408–416.

Shi, J., D. R. Williams et al. (2008). A script-assisted microscopy (SAM) package to improve data acquisition rates on FEI Tecnai electron microscopes equipped with Gatan CCD cameras. *J Struct Biol* **164**(1): 166–169.

Sorzano, C. O., C. Messaoudi et al. (2009). Marker-free image registration of electron tomography tilt-series. *BMC Bioinformatics* **10**: 124.

Stahlberg, H. (2012). ctf-simulation, Centre of Cellular Imaging and Nanoanalytics, http://www.c-cina.unibas.ch/download/ctf-simulation, accessed in 2013.

Stark, H., F. Zemlin et al. (1996). Electron radiation damage to protein crystals of bacteriorhodopsin at different temperatures. *Ultramicroscopy* **63**: 75–79.

Stewart, P. L., S. D. Fuller et al. (1993). Difference imaging of adenovirus: Bridging the resolution gap between X-ray crystallography and electron microscopy. *EMBO J* **12**(7): 2589–2599.

Suloway, C., J. Pulokas et al. (2005). Automated molecular microscopy: The new Leginon system. *J Struct Biol* **151**(1): 41–60.

Tang, J., G. C. Lander et al. (2011). Peering down the barrel of a bacteriophage portal: The genome packaging and release valve in p22. *Structure* **19**(4): 496–502.

Taylor, K. A. and R. M. Glaeser (1973). Hydrophilic support films of controlled thickness and composition. *Rev Sci Instrum* **44**(10): 1546–1547.

Taylor, K. A. and R. M. Glaeser (1974). Electron diffraction of frozen, hydrated protein crystals. *Science* **186**(4168): 1036–1037.

Thuman-Commike, P. A., H. Tsuruta et al. (1999). Solution x-ray scattering-based estimation of electron cryomicroscopy imaging parameters for reconstruction of virus particles. *Biophys J* **76**(4): 2249–2261.

Tivol, W. F., A. Briegel et al. (2008). An improved cryogen for plunge freezing. *Microsc Microanal* **14**(5): 375–379.

Topf, M., K. Lasker et al. (2008). Protein structure fitting and refinement guided by cryo-EM density. *Structure* **16**(2): 295–307.

Toyoshima, C. (1989). On the use of holey grids in electron microscopy. *Ultramicroscopy* **30**: 439–444.

Toyoshima, C. and N. Unwin (1988). Contrast transfer for frozen-hydrated specimens—Determination from pairs of defocused images. *Ultramicroscopy* **25**(4): 279–291.

Tran, E. E., M. J. Borgnia et al. (2012). Structural mechanism of trimeric HIV-1 envelope glycoprotein activation. *PLoS Pathog* **8**(7): e1002797.

Trinick, J. and J. Cooper (1990). Concentration of solutes during preparation of aqueous suspensions for cryo-electron microscopy. *J Microsc* **159**: 215–222.

Unwin, N. (2005). Refined structure of the nicotinic acetylcholine receptor at 4Å resolution. *J Mol Biol* **346**(4): 967–989.

Unwin, P. N. and R. Henderson (1975). Molecular structure determination by electron microscopy of unstained crystalline specimens. *J Mol Biol* **94**(3): 425–440.

van der Heide, P., X. P. Xu et al. (2007). Efficient automatic noise reduction of electron tomographic reconstructions based on iterative median filtering. *J Struct Biol* **158**(2): 196–204.

Veesler, D., T. S. Ng et al. (2013). Atomic structure of the 75 MDa extremophile Sulfolobus turreted icosahedral virus determined by CryoEM and X-ray crystallography. *Proc Natl Acad Sci USA* **110**(14): 5504–5509.

Vogel, R. H., S. W. Provencher et al. (1986). Envelope structure of Semliki Forest virus reconstructed from cryo-electron micrographs. *Nature* **320**(6062): 533–535.

Vonck, J. (2000). Parameters affecting specimen flatness of two-dimensional crystals for electron crystallography. *Ultramicroscopy* **85**(3): 123–129.

Wade, R. H. (1992). A brief look at imaging and contrast transfer. *Ultramicroscopy* **46**: 145–156.

Walker, M., J. Trinick et al. (1995). Millisecond time resolution electron cryo-microscopy of the M-ATP transient kinetic state of the acto-myosin ATPase. *Biophys J* **68**(4 Suppl.): 87S–91S.

Wang, G. J., C. Porta et al. (1992). Identification of a Fab interaction footprint site on an icosahedral virus by cryoelectron microscopy and X-ray crystallography. *Nature* **355**(6357): 275–278.

White, H. D., M. L. Walker et al. (1998). A computer-controlled spraying-freezing apparatus for millisecond time-resolution electron cryomicroscopy. *J Struct Biol* **121**(3): 306–313.

Wilson, N. R., P. A. Pandey et al. (2009). Graphene oxide: Structural analysis and application as a highly transparent support for electron microscopy. *ACS Nano* **3**(9): 2547–2556.

Wolf, M., R. L. Garcea et al. (2010). Subunit interactions in bovine papillomavirus. *Proc Natl Acad Sci USA* **107**(14): 6298–6303.

Wynne, S. A., R. A. Crowther et al. (1999). The crystal structure of the human hepatitis B virus capsid. *Mol Cell* **3**(6): 771–780.

Xie, Q., M. Spilman et al. (2013). Electron microscopy analysis of a disaccharide analog complex reveals receptor interactions of adeno-associated virus. *J Struct Biol* **184**(2): 129–135.

Yang, C., G. Ji et al. (2012). Cryo-EM structure of a transcribing cypovirus. *Proc Natl Acad Sci USA* **109**(16): 6118–6123.

Yu, X., P. Ge et al. (2011). Atomic model of CPV reveals the mechanism used by this single-shelled virus to economically carry out functions conserved in multishelled reoviruses. *Structure* **19**(5): 652–661.

Yu, X., L. Jin et al. (2008). 3.88 Å structure of cytoplasmic polyhedrosis virus by cryo-electron microscopy. *Nature* **453**(7193): 415–419.

Yu, X., L. Jin et al. (2013). 3.5Å cryoEM structure of Hepatitis B virus core assembled from full-length core protein. *PLoS One* **8**(9): e69729.

Zemlin, F., K. Weiss et al. (1978). Coma-free alignment of high-resolution electron-microscopes with aid of optical diffractograms. *Ultramicroscopy* **3**(1): 49–60.

Zernike, F. (1942). Phase contrast, a new method for the microscopic observation of transparent objects Part II. *Physica* **9**: 974–986.

Zhang, P., M. J. Borgnia et al. (2003). Automated image acquisition and processing using a new generation of 4K × 4K CCD cameras for cryo electron microscopic studies of macromolecular assemblies. *J Struct Biol* **143**(2): 135–144.

Zhang, R., C. F. Hryc et al. (2011). 4.4 Å cryo-EM structure of an enveloped alphavirus Venezuelan equine encephalitis virus. *EMBO J* **30**(18): 3854–3863.

Zhang, X., P. Ge et al. (2013a). Cryo-EM structure of the mature dengue virus at 3.5-Å resolution. *Nat Struct Mol Biol* **20**(1): 105–110.

Zhang, X., H. Guo et al. (2013b). A new topology of the HK97-like fold revealed in Bordetella bacteriophage by cryoEM at 3.5 Å resolution. *Elife* **2**(0): e01299.

Zhang, X. and Z. Hong Zhou (2011). Limiting factors in atomic resolution cryo electron microscopy: No simple tricks. *J Struct Biol* **175**: 253–263.

Zhang, X., L. Jin et al. (2010). 3.3 Å cryo-EM structure of a nonenveloped virus reveals a priming mechanism for cell entry. *Cell* **141**(3): 472–482.

Zhang, X., E. Settembre et al. (2008). Near-atomic resolution using electron cryomicroscopy and single-particle reconstruction. *Proc Natl Acad Sci USA* **105**(6): 1867–1872.

Zhang, X., S. Sun et al. (2012). Structure of Sputnik, a virophage, at 3.5-Å resolution. *Proc Natl Acad Sci USA* **109**(45): 18431–18436.

Zhu, J., L. Cheng et al. (2010). Building and refining protein models within cryo-electron microscopy density maps based on homology modeling and multiscale structure refinement. *J Mol Biol* **397**(3): 835–851.